

XID+PRIMA, II: STEPPING THROUGH HYPERSPECTRAL IMAGING TO DEBLEND PRIMAGER BEYOND THE EXTRAGALACTIC CONFUSION LIMIT

J. M. S. DONNELLAN,¹ B. PAUTASSO,¹ S. J. OLIVER,¹ M. BÉTHERMIN,² L. BING,¹ A. BOLATTO,³ L. CIESLA,⁴ D. KOOPMANS,^{5,6} A. POPE,⁷ S. SERJEANT,⁸ L. WANG^{5,6}¹Astronomy Centre, University of Sussex, Falmer, Brighton BN1 9QH, UK²Université de Strasbourg, CNRS, Observatoire astronomique de Strasbourg, UMR 7550, 67000 Strasbourg, France³Department of Astronomy, University of Maryland, College Park, MD 20742, USA⁴Aix Marseille Univ, CNRS, CNES, LAM, Marseille, France⁵SRON Netherlands Institute for Space Research, Landleven 12, 9747 AD Groningen, The Netherlands⁶Kapteyn Astronomical Institute, University of Groningen, Postbus 800, 9700 AV Groningen, The Netherlands⁷Department of Astronomy, University of Massachusetts, Amherst, MA 01003, USA⁸School of Physical Sciences, The Open University, Walton Hall, Milton Keynes, MK7 6AA, UK*Version December 16, 2025*

ABSTRACT

The PRobe far-Infrared Mission for Astrophysics (PRIMA) concept aims to map large areas with spectral coverage and sensitivities inaccessible to previous FIR space telescopes, covering 25–235 μm . We synthesise images representing a deep imaging survey, with realistic instrumental and confusion noise, reflecting the latest PRIMAgger instrument specifications. We present a new Bayesian modelling approach **XID+stepwise** that exploits PRIMAgger’s hyperspectral imaging to derive self-consistent, informative flux priors by sequentially propagating constraints from short to long wavelengths. With Euclid-like prior source positions, this method recovers fluxes to within 20% down to 0.2–0.7 mJy across 45–84 μm , which correspond to factors of 1.3–3.4 fainter than the confusion limit. For the most confusion-dominated channels, accurate fluxes are measured down to 0.9, 2.5, 7.6 and 14.8 mJy at 92, 126, 183 and 235 μm , respectively, which are factors of 3–5 better than the confusion limit. Using a deeper Euclid-based prior catalogue and weak ancillary flux priors at 25 μm yields further improvements, reaching up to a factor ~ 7 fainter than the confusion limit at 96 μm . Additionally, we demonstrate that positional priors from blind source detection followed by deblending via **XID+** enables PRIMAgger to achieve sensitivity beyond the confusion limits using PRIMAgger data alone. We show that IR-luminous galaxies at $z \sim 2$ are robustly detected in a large fraction of the PRIMAgger channels ($>98\%$ in 12 out of the 16 considered channels), providing dense sampling of the FIR SED even for sources several factors below the classical confusion limit. We explore the impact on our results for a range of systematic effects, including cirrus contamination, optical degradation, and calibration uncertainties. These findings indicate that confusion noise will not limit the key science from PRIMA extragalactic imaging surveys when employing **XID+**.

1. INTRODUCTION

Observing galaxies at Far-Infrared (FIR) wavelengths is crucial to understanding the physical processes that govern their evolution. Dust within galaxies is a key component of the interstellar medium (ISM, [Draine 2011](#)) and can reprocess a significant fraction of the UV emission from hot massive stars, which trace star formation, into the FIR ([Madau & Dickinson 2014](#)). As a result, the peak of a galaxy’s spectral energy density (SED) falls within the FIR wavelength range ($\sim 100 \mu\text{m}$ rest-frame). From this reprocessing by dust, roughly half of the total extragalactic background light originates from the infrared emission we receive from galaxies, known as the cosmic infrared background (CIB, [Puget et al. 1996](#)), despite dust only making up a fraction of the total baryonic mass of a galaxy ([Hauser & Dwek 2001](#); [Dole et al. 2006](#)). Since the FIR emission is proportional to the obscured star-formation rate (SFR, [Kennicutt 1998](#)), this leads to a substantial fraction of the total SFR density

of the universe being obscured by dust, particularly during the peak epoch when most stars were formed (cosmic noon: $z \sim 2$, [Dunlop et al. 2017](#); [Zavala et al. 2021](#)).

Galactic dust also significantly changes how we observe galaxies through the attenuation of rest-frame UV-NIR emission, whereby dust absorbs and scatters light into and out of the line-of-sight. It is crucial to correct for this in order to avoid biases in the determination of physical properties of galaxies, such as the stellar mass, SFR, age and metallicity ([Cardelli et al. 1989](#); [Calzetti et al. 2000](#)). Different star-dust geometries, dust grain types and sizes can also significantly alter the attenuation (see [Salim & Narayanan \(2020\)](#) for a review). As such, comprehensive sampling of a galaxy’s SED from the UV to FIR is required in order to better constrain this attenuation, particularly when applying SED-fitting techniques to determine galaxy properties (see reviews by [Walcher et al. 2011](#); [Conroy 2013](#)). Moreover, dense sampling across the peak of the SED is required to accurately determine

IR luminosity, dust mass and dust temperature (Casey 2012; Farrah et al. 2025). Good coverage of the MIR-FIR range captures and constrains emissions from polycyclic aromatic hydrocarbons (PAHs) and warm dust (see reviews by Casey et al. 2014; Li 2020), whilst also significantly helping to discriminate between contributions to a galaxy’s SED from star-formation and Active Galactic Nuclei (AGN, Pope et al. 2008; Mullaney et al. 2011).

Currently, the James Webb Space Telescope (JWST) probes the rest-frame UV-MIR and MIRI has been used to begin constraining PAH evolution and dust luminosities of galaxies out to $z \sim 2$ (e.g. Shvai et al. 2024). However, JWST is limited to relatively small area surveys (< 0.4 sq. deg. surveyed with MIRI in deep extragalactic fields the first 4 years of JWST) and can only observe up to ~ 25 μm . The Atacama Large Millimetre Array (ALMA), on the other hand, primarily probes the sub-millimetre regime ($\gtrsim 300$ μm) and can detect dust-obscured star-forming galaxies out to the highest redshifts (Fudamoto et al. 2020; Gruppioni et al. 2020; Inami et al. 2022), but is also limited in its small field of view. Previous space-based FIR observatories such as Herschel and Spitzer filled the wavelength coverage gap between JWST and ALMA before ending observations over a decade ago, but these were limited in both spectral sampling capabilities and sensitivity.

To bridge the current sensitivity and wavelength gap between JWST and ALMA, the PRobe Far-Infrared Mission for Astrophysics (PRIMA, Glenn et al. 2025) has been proposed. PRIMA is a 1.8 m space-based telescope which will be cryogenically-cooled to 4.5 K and has two planned instruments: the Far-Infrared Enhanced Survey Spectrometer (FIRESS, Bradford et al. 2025) and the PRIMA Imager (PRIMAgger, Ciesla et al. 2025). FIRESS provides continuous spectral coverage from 24 to 235 μm in two spectral resolution modes ($R \geq 85$ and $R = 4400(112 \mu\text{m}/\lambda)$). PRIMAgger will perform imaging via two modes, with the first providing hyperspectral imaging with $R \sim 8$ linear variable filters (LVFs) from 24 to 84 μm . The second provides both intensity and polarimetric imaging via four broadband filters from 92 to 235 μm .

Both FIRESS and PRIMAgger will provide significant sensitivity, mapping speed and wavelength coverage improvements compared to previous FIR observatories. These will allow PRIMA to conduct large area extragalactic surveys (tens of sq. deg.), comprehensively sampling the entire FIR SED of a large sample of galaxies throughout the MIR-FIR range out to $z \sim 4$ (Burgarella et al. 2025; Boquien et al. 2025). In particular, it will enable the study of PAH emission (Yoon et al. 2025), constrain the dust-mass function (Traina et al. 2025), reveal dust-obscured AGN (Donnan et al. 2025; Barchiesi et al. 2025) and shed light on the co-evolution of supermassive black holes (SMBHs) and their host galaxies (Faisst et al. 2025; Fernández-Ontiveros et al. 2025). Many other applications exploiting the capabilities of PRIMA have also been identified by the wider astronomy community (Mouillet et al. 2023, 2025).

In order to realise the full benefit from these gains in sensitivity in extragalactic imaging surveys with PRIMAgger, it will be essential to reduce the impact of confusion noise. Confusion noise limits the depth reached in FIR imaging data for space-based, single-dish observato-

ries due to the limited mirror size (Condon 1974). For a given mirror size, the angular resolution of the telescope decreases as wavelength increases, leading to the blurring of sources when the telescope beam is large compared to the average separation of those sources. Confusion noise, for example, limited Herschel surveys to detect only the most extreme sources at high redshift (Nguyen et al. 2010).

Béthermin et al. (2024) (hereafter referred to as B24) demonstrated that PRIMAgger will be confusion-noise limited at wavelengths of $\lambda \gtrsim 45 \mu\text{m}$ for its deep extragalactic surveys. However, Donnellan et al. (2024) (referred to as D24) demonstrated that accurate flux measurements could be obtained below the confusion limits of simulated PRIMAgger maps. This was achieved by employing XID+ (Hurley et al. 2017), a deblending tool which uses a probabilistic Bayesian framework which includes prior information of galaxy positions and fluxes to obtain the full posterior probability distributions of fluxes for those galaxies. It has previously been used to perform source extraction for the Herschel Extragalactic Legacy Project (HELP; Shirley et al. 2019, 2021). Additional works showed that by applying prior flux information, e.g. from SED-fitting of ancillary photometry, further gains in flux accuracy and depth could be achieved (Pearson et al. 2017, 2018; Wang et al. 2021, 2024). D24 found positional catalogues of high completeness coupled with weak prior flux information provided up to an order of magnitude improvement in source flux recovery relative to the confusion limits of simulated PRIMAgger maps. However, the prior flux information used in D24 was idealised, taking the true values of the simulation using a toy model, along with a physically unmotivated positional prior source catalogue.

In this work, we set out to build upon the work of D24 and fully utilise the hyperspectral capabilities of PRIMAgger to demonstrate that accurate prior flux knowledge can be obtained from the PRIMAgger data itself. We show that these informative flux priors can be used to deblend confusion-limited PRIMAgger maps starting with realistic Euclid-based prior source catalogues to obtain accurate flux measurements for galaxies well below the confusion limit. Additionally, we update our simulations to reflect the latest PRIMAgger specifications (Ciesla et al. 2025), and investigate the impact of various systematics, such as galactic cirrus and calibration effects, on our results.

This paper is structured as follows. In Section 2, we outline how the simulated PRIMAgger maps are generated and highlight the sources of various systematics. Section 3 describes the construction of positional prior source catalogues and the methodology of obtaining prior flux information. Our main results are presented in Section 4 along with the impact of systematics. We then discuss the implications of our results in Section 5 and make final conclusions in Section 6.

2. SIMULATIONS

To evaluate the flux-recovery performance of PRIMAgger in extragalactic observations, we generate model FIR observations. The model observation is composed of three components: the extragalactic sky (Section 2.1), foreground emissions (Section 2.2), and the characteristics of PRIMAgger itself (Section 2.3). These components

are combined to produce a semi-realistic observation, on which we perform flux recovery tests.

2.1. Extragalactic Sky

We utilise the Simulated Infrared Dusty Extragalactic Sky (SIDES¹; Béthermin et al. 2017, 2022; Gkogkou et al. 2023) to model the FIR extragalactic sky. We refer interested readers to these papers for details, but provide a brief summary here.

Originally presented in Béthermin et al. (2017), SIDES is a semi-empirical simulation of the FIR and millimetre extragalactic sky. Built upon the Bolshoi-Planck dark matter simulation (Klypin et al. 2016; Rodríguez-Puebla et al. 2016), it populates dark matter haloes with galaxies using an abundance-matching technique.

The resulting light-cone catalogue contains 5.6 million galaxies over an area of 1.96 deg^2 spanning $0 < z < 10$. Gkogkou et al. (2023) applied the same methodology to the Uchuu simulation (Ishiyama et al. 2021) to construct a larger 117 deg^2 light-cone catalogue covering $0 < z < 7$. We select a 2 deg^2 region from this latter catalogue for our work.

Although we do not yet make full use of the large area of the updated SIDES catalogue, its large area enables the study of cosmic variance (e.g. Gkogkou et al. 2023, references therein) and the training of machine learning models (e.g. Lauritsen et al. 2021, Koopmans et al. submitted) in the future.

2.2. Foreground emissions

Observations of extragalactic sources in the FIR are contaminated by two components of foreground emission: zodiacal dust and galactic cirrus (Low et al. 1984).

Zodiacal dust emission arises from the thermal re-radiation of absorbed solar radiation by warm interplanetary dust, with its spectrum peaking in the MIR ($\sim 10 \text{ }\mu\text{m}$; Leinert et al. 1998; Hauser et al. 1998). Although we acknowledge the impact it would have on our observations, particularly in the bluer PRIMAgger channels, we do not model it in this work. We justify its omission since it varies over scales much larger than a point source, and it should be possible to accurately remove its contribution.

Galactic cirrus emission is produced by the thermal re-radiation of the energy flux from the ambient interstellar radiation field by much cooler interstellar dust. Due to the lower temperature, its emission peaks in the FIR ($\sim 150 \text{ }\mu\text{m}$; Draine 2003; Zubko et al. 2004).

2.2.1. Modelling cirrus

We utilise the IRIS (Miville-Deschénes & Lagache 2005) $100 \text{ }\mu\text{m}$ maps to predict the cirrus intensity (I_{100}) in several proposed PRIMAgger deep fields. After correcting the maps for residual zodiacal light and CIB contamination following Miville-Deschénes et al. (2007), we find the considered fields lie in regions of low cirrus, with intensities ranging from 0.4 to 2.6 MJy sr^{-1} . To cover a range of potential cirrus conditions, we model three cirrus intensities: 0.5, 1.5, and 2.5 MJy sr^{-1} .

We adopt Fractional Brownian motion (fBm) as a common, if crude, method used to simulate cirrus emissions

(e.g. Miville-Deschénes et al. 2007, references therein). Although capable of replicating the self-similar nature of cirrus, it fails at producing the large-scale filamentary structures observed in real cirrus since the phase distribution of the fBm map is random. However, since our analysis is principally concerned with fluctuations on or around the scale of point sources, and not those on larger scales, we adopt a fBm model as a suitable clumpy background to represent the effects of cirrus. Further discussion of fBm is provided in Appendix A (Figure A1).

The structure map produced by the fBm process is generated in arbitrary units, normalised between 0 and 1. To construct an intensity map, we scale the structure map such that variance at the scale of a point source matches the Gautier et al. (1992) prediction, applying the corrections suggested in Miville-Deschénes et al. (2007) for low intensity ($I_{100} < 10 \text{ MJy sr}^{-1}$) regions. We additionally scale the intensity to the appropriate wavelength using the interstellar dust SED from Zubko et al. (2004).

2.3. PRIMAgger

As mentioned previously, PRIMAgger will operate in two imaging modes. PHI uses linear variable filters (LVFs) to conduct hyperspectral imaging between 24 and $84 \text{ }\mu\text{m}$ at a spectral resolution of $R = \lambda/\Delta\lambda \geq 8$, divided into two bands (PHI1 and PHI2), whilst PPI provides intensity and polarimetric imaging across four bands with $R \approx 4$, covering 92 to $235 \text{ }\mu\text{m}$ (Ciesla et al. 2025).

2.3.1. PHI

The two PHI bands span 24–45 and 45– $84 \text{ }\mu\text{m}$ respectively. In D24, each PHI band was approximated by 6 broad channels with $R = 10$, each consisting of a tophat filter and a Gaussian beam.

With the development of the LVF (Jellema et al. 2024, Jellema et al. in prep), more realistic simulations of the filter transmissions than were used in D24 are now available. The achieved profile is the result of a compromise between high spectral resolution and low out-of-band power. In this work, we assume 52 logarithmically-sampled simulated filter profiles (26 per band), each with a spectral resolution of $R = 8$ and a profile aimed to be as close as possible to a tophat (Figure 1). Further developments of the modelling of PHI spectral sampling and filter profile will be provided in Ciesla et al. (in prep).

More realistic optical modelling of the telescope beams has now been carried out. Each filter now has a corresponding Airy disc beam which have been modified to include the central and tripod obscuration and the coupling of the optics with the detectors (Jellema et al. in prep).

To improve signal-to-noise and reduce computational cost, we coadd nearby filter to form 12 channels comparable to those used in D24. This procedure is illustrated in Figure 1.

2.3.2. PPI

In D24, the four PPI bands were modelled with tophat filters and Gaussian beams. In this work, the filters remain tophats, although PPI1 and PPI3 have been shifted to avoid prominent emission lines. As with PHI, the beams are now modelled as Airy discs to more accurately reflect the telescope's optics. Figure B1 shows the

¹ <https://data.lam.fr/sides/home>

TABLE 1
PRIMAGER CHANNEL PROPERTIES AND DETECTION LIMITS

Channel	Peak Wavelength (λ_{peak}) [μm]	Filter FWHM [μm]	Spectral Resolution (R)	Beam FWHM ["]	Point Source Sensitivity ($5\sigma_{\text{inst}}$) [μJy]	Confusion Limit ($5\sigma_{\text{conf}}$) [μJy]
PHI1_1	25.0	3.6	7.1	4.1	100	45
PHI1_2	27.8	4.2	6.7	4.3	111	50
PHI1_3	31.1	4.5	7.1	4.6	124	61
PHI1_4	34.3	4.9	7.1	4.9	137	75
PHI1_5	37.9	5.4	7.1	5.2	151	98
PHI1_6	42.3	6.4	6.7	5.7	169	134
PHI2_1	47.3	6.8	7.1	6.2	189	300
PHI2_2	52.1	7.5	7.1	6.7	208	414
PHI2_3	58.2	8.8	6.7	7.3	233	633
PHI2_4	65.0	9.3	7.1	8.0	260	967
PHI2_5	71.8	10.3	7.1	8.8	287	1450
PHI2_6	80.0	12.1	6.7	9.7	320	2310
PPI1	92.0	23	4.0	11.6	145	4090
PPI2	126	32	3.9	15.0	209	12900
PPI3	183	46	4.0	20.3	294	32100
PPI4	235	58	4.1	27.6	375	45200

NOTE. — Details of the 12 representative PRIMager channels for the two hyperspectral bands, PHI1 and PHI2, and the four polarimetry broadband channels, PPI1-PPI4. Peak wavelength and FWHM are given for each channel. For PPI, where the filters are modelled as tophats, we instead cite their range. Spectral resolution of each channel is defined as $R = \lambda_{\text{peak}}/\text{FWHM}$. Beam FWHMs are estimated for the baseline telescope aperture (1.8 m) and detector and pixel layout. The point source sensitivities are given for a deep survey observed for ~ 1500 hr deg $^{-2}$ in the absence of confusion. The classical confusion limits are estimated following B24.

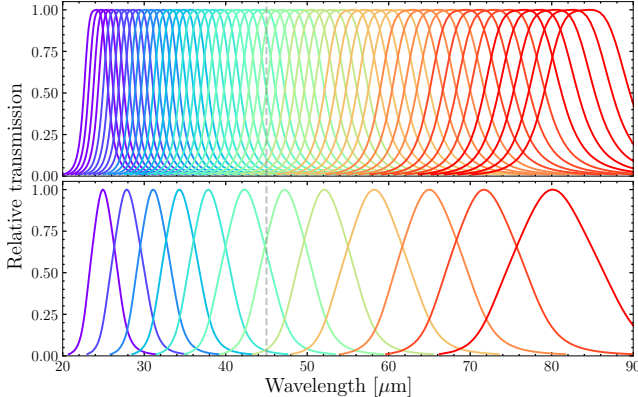


FIG. 1.— Filter transmission curves of all PHI channels, both narrow (top) and coadded (bottom). The filters are coloured to match their associated coadded channel.

2D and radial profiles for three representative PRIMager channels, PHI1_1, PHI2_1, and PPI1.

A summary of the 16 PRIMager channels used in this work (12 for PHI and four for PPI) is given in Table 1.

2.4. Observations and Mapmaking

We convert the light-cone catalogue into sky maps using the SIDES Python mapmaker (Béthermin et al. 2022). To summarise, the flux of each source is placed at the centre of its pixel, and then convolved with the telescope beams described previously. This process is repeated for each channel, using map pixels of 0.8, 1.3, and 2.3' for PHI1, PHI2, and PPI respectively.

The resulting maps include confusion noise, which arises from the convolution of sources with the telescope beam (Condon 1974), but not instrumental noise². We

² We include under instrumental noise any non-confusion sources of noise, including the detectors and photon statistics, but exclude

refer to these maps as ‘noiseless’.

Following B24, the confusion noise (σ_{conf}) is defined via an iterative 5σ clipping process. The mode and standard deviation of the noiseless maps are measured, positive 5σ outliers are masked, and the standard deviation is recomputed. This process is repeated until the standard deviation converges, defining σ_{conf} . The classical confusion limit is then defined as $5\sigma_{\text{conf}}$.

We model observations representative of a deep PRIMager survey (~ 1500 hr deg $^{-2}$), predicted to reach point source sensitivities ($5\sigma_{\text{inst}}$) of 124, 233, 145, 209, 294, 375 in PHI1, PHI2, PPI1, PPI2, PPI3, PPI4 respectively. White Gaussian instrumental noise is added on a per pixel level, based on the predicted sensitivities. Whilst spatially uncorrelated noise is unrealistic, we confirm our pixel noise yields the correct point source performance. A more realistic instrumental noise model, alongside a more sophisticated map making algorithm is the subject of current and future work. Maps containing both confusion and instrumental noise are referred to as ‘noisy’ hereafter. We emphasise that these noise maps do not include any cirrus emission. Unless otherwise stated, all analysis in this paper is performed on these maps (Figure 2).

In addition to these maps, which will form the basis of our main results, we produce several non-nominal maps to investigate the impact of several systematics on our flux recovery.

2.4.1. Cirrus-contaminated maps

We create observations where cirrus is present at the aforementioned intensities. We add cirrus to the noisy maps for channels redwards of PHI2_3 (see Figure 3).

For these maps we apply a simple local background

any foreground emissions.

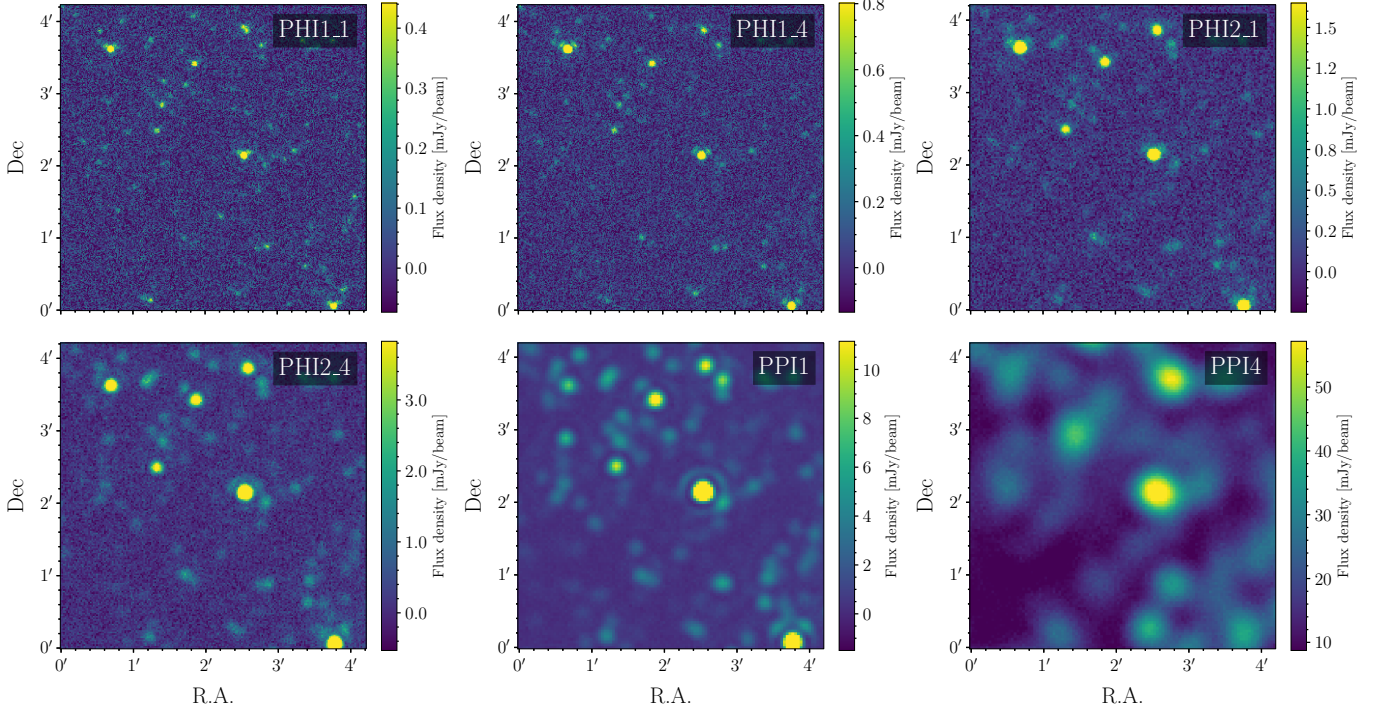


FIG. 2.— Cutouts of simulated observations including both instrumental and confusion noise for six representative PRIMAGER channels. The transition between instrumental and confusion noise dominating is apparent. Each cutout covers an area of $4.24 \times 4.24'$. The instrumental noise is added on a per pixel level representative of a deep ($\sim 1500 \text{ hr deg}^{-2}$) survey, and is discussed in 2.4.

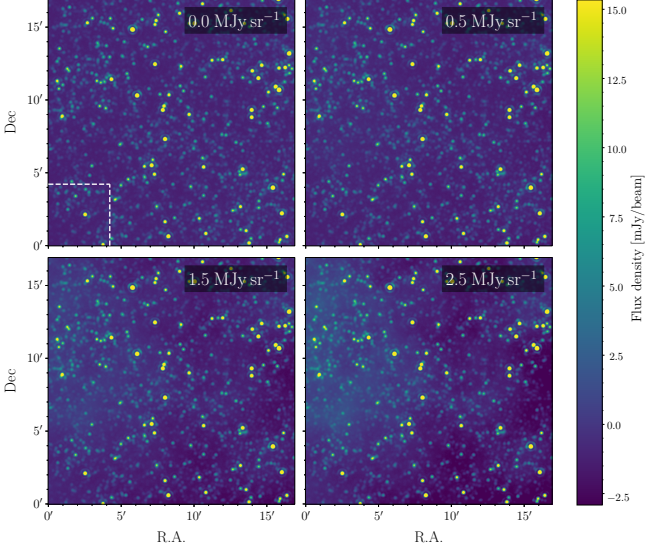


FIG. 3.— Cutouts of simulated observations in PPI1 in the presence of various cirrus levels. All cutouts share the same colour scale, are mean-subtracted, and span $34 \times 34'$. The bounded area in the top left panel corresponds to the area shown in Figure 2.

subtraction filter, modelled after Nebuliser³ following the procedure outlined in Valiante et al. (2016). Further discussion on this procedure is provided in Appendix A, and the impact of cirrus on our flux recovery is discussed in Section 4.3.

2.4.2. Non-nominal beams

We consider various scenarios which would result in non-nominal telescope beams.

³ <http://casu.ast.cam.ac.uk/surveys-projects/software-release>

Firstly, we consider the effect of wider beams on our flux recovery. This could, for example, be the result of a smaller telescope aperture or optical aberrations. We parametrise this following:

$$\text{FWHM}_{\text{degraded}} = 1.1\sqrt{(\text{FWHM}_{\text{nominal}}^2 + c^2)}, \quad (1)$$

where $c = 3''.65$, and $\text{FWHM}_{\text{nominal}}$ and $\text{FWHM}_{\text{degraded}}$ is the FWHM of the nominal and degraded beams respectively. We create these beams by broadening the nominal beams with a Gaussian to reach the target width, and refer to them as ‘degraded’ hereafter.

Secondly, we consider that reaching the target sensitivities for a survey such as the one considered here will require stacking hundreds of independent sky scans. Small astrometric errors in each scan, predicted to have an RMS of $0''.7$ per axis, would result in the effective beam being broadened. To mimic this effect, we convolve our beams with a 2D Gaussian of $\sigma = 0''.7$ (FWHM = $1''.65$), we refer to these beams as ‘jittered’.

Finally, we construct simplified beams to investigate the effect of miscalibrations on our flux recovery. These beams are modelled as perfect Airy discs,

$$I(r) = I_0 \left(\frac{2J_1(kr)}{kr} \right)^2, \quad (2)$$

where $I(r)$ is the radial beam profile, I_0 is the peak intensity, J_1 is the first order Bessel function of the first kind, k is a band-dependent parameter controlling the beam width, and r is the radial distance from the beam centre, $r^2 = x^2 + y^2$. For each band, k is chosen such that the resulting beam has the same FWHM as the nominal beam. Although these beams lack the realistic optical features present in our nominal beams, they allow us to

independently vary the beam parameters with high fidelity (see Section 3.4). These beams will be referred to as ‘simplified’ hereafter. A comparison of the radial profiles between the nominal and simplified beams is shown in Figure B1.

For each of these three non-nominal beam scenarios, we construct new noisy maps to run XID+.

3. XID+

3.1. XID+: A Probabilistic De-Blender

XID+⁴ is a prior-based source photometry tool developed by Hurley et al. (2017). It estimates the fluxes of a collection of sources with known positions simultaneously. The XID+ model assumes that the input data (\mathbf{d}) are maps with $n_1 \times n_2 = M$ pixels, where the maps are formed from N known sources, with flux densities \mathbf{S}_i and a single global background term, B , accounting for unknown sources. The point response function (PRF, \mathbf{P}) quantifies the contribution each source makes to the pixels in the map and is estimated from the point spread function (PSF) of the observatory and instrument optical system, which is assumed to be known a priori. In this case the PRF is the same for each source and centred on the centre of the pixel containing the source, in the same way that the simulations were constructed. The map can therefore be described as follows:

$$\mathbf{d} = \sum_{i=1}^N \mathbf{P} \mathbf{S}_i + N(0, \Sigma_{\text{inst}}) + N(B, \Sigma_{\text{conf}}), \quad (3)$$

where the two independent noise terms represent the instrumental noise and the residual confusion noise which is modelled as Gaussian fluctuations about the global background. XID+ undertakes an adaptive form of Hamiltonian Monte Carlo sampling, the no-u-turn sampler (NUTS) sampling, from this probabilistic model to obtain the full posterior. Hurley et al. (2017) utilised the Bayesian inference tool, Stan, however, here we build the Numpyro backend into XID+ to improve speed.

3.2. Positional priors

As input, XID+ requires the positions of sources at which the deblending should be performed and their fluxes estimated. These positional priors can be obtained by performing source detection on the PRIMAgger maps themselves or from ancillary data such as source catalogues constructed from optical surveys at higher angular resolution. In the following, we consider both of these methods.

3.2.1. Euclid prior catalogues

By the time PRIMA is scheduled to launch, Euclid is expected to have completed observations of both its Wide and Deep Field surveys (with preliminary data already released: Euclid Collaboration: Aussel et al. 2025). As such, a wealth of deep optical and NIR photometry will be available for galaxies within most regions of sky likely to be covered by PRIMA, along with robust estimates of their redshifts and stellar masses (Euclid Collaboration: Tucci et al. 2025). Considering this, we investigate

⁴ https://github.com/H-E-L-P/XID_plus

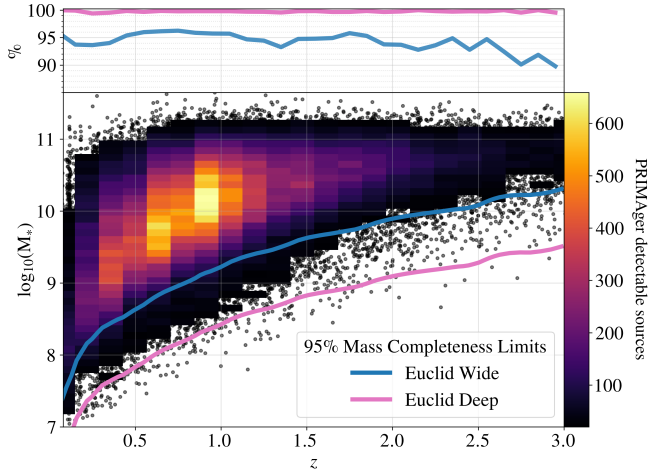


FIG. 4.— Distribution of SIDES sources which are above the point source sensitivity in at least 5 of the PRIMAgger bands. **Bottom:** Stellar mass-redshift distribution of the PRIMAgger detectable sources within SIDES relative to the Euclid Q1 95% stellar mass completeness limit from Euclid Collaboration: Enia et al. (2025) (solid blue curve), representing a Euclid Wide Field survey depth and a 0.8 dex deeper Euclid Deep Field Survey (solid pink curve). **Top:** The percentage of PRIMAgger detectable sources in SIDES which are above the mass completeness limits for the respective Euclid survey depths.

the performance of XID+ for sources within the SIDES simulation which are representative of those that will be detected by the Euclid extragalactic surveys.

Ideally, we would utilise simulated Euclid photometry within SIDES to determine which sources should be kept to construct a proxy, Euclid-like source catalogue. However, SED information for individual sources within SIDES only extends down to MIR wavelengths. Instead, we apply a stellar mass and redshift cut to the master SIDES catalogue based on the 95% stellar mass completeness limit derived from the Euclid Q1 data release (Euclid Collaboration: Enia et al. 2025). This is shown in Figure 4 as the solid blue curve and is referred to as Euclid Wide since the Q1 data release is of the same depth in magnitude as the Wide Field survey depth. It is expected that the Euclid Deep Field Survey will be ~ 2 magnitudes deeper in apparent magnitude than the Wide survey (Laureijs et al. 2011; Euclid Collaboration: Scaramella et al. 2022). This should correspond to the stellar mass completeness being 0.8 dex deeper in stellar mass and we show this with the solid pink curve (denoted as Euclid Deep). All SIDES sources above these respective limits form the prior source catalogues (hereafter referred to as Euclid Wide and Euclid Deep) for which the deblending will be performed. The stellar mass completeness limit of Euclid Collaboration: Enia et al. (2025) was only derived up to $z = 3$. Subsequently, we have extrapolated this relation for higher redshifts by fitting a broken power law. However, there are very few sources at these high redshifts within SIDES which significantly contribute flux to the PRIMAgger maps. Therefore, any error in this extrapolation will have a negligible effect.

The exact positions of the sources within the simulated maps are used. However, we explore the impact of positional offsets on the modelling accuracy in Section 4.3.

The bottom panel of Figure 4 also shows the stellar mass vs. redshift distribution of the SIDES sources within the 2 deg^2 light-cone which are above the point

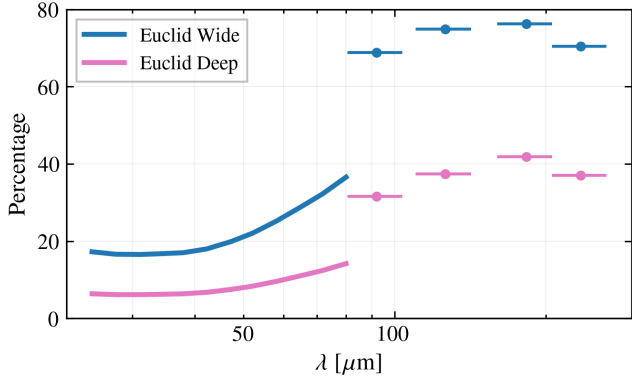


FIG. 5.— Percentage of sources within the Euclid prior catalogues which are above the instrument point source sensitivity at each of the PRIMAGER channels for the considered survey. At the shortest wavelengths, less than 20% of the sources within the prior catalogues are detectable above the point source sensitivities and significantly contributing flux to the maps.

source sensitivity of the considered PRIMAGER survey depth in at least 5 of the PRIMAGER bands. These sources are effectively the main contributors of flux to the PRIMAGER maps and are thus referred to as PRIMAGER-detectable sources. As the top panel of Figure 4 shows, 90–95% of these sources are above the Euclid Wide stellar mass limit, and therefore are present in the Euclid Wide prior source catalogue, out to $z \sim 3$. For the Euclid Deep prior catalogue, effectively all PRIMAGER-detectable sources are present.

Due to the impressive depths in stellar mass reachable with Euclid, there can be significant fractions of sources within the prior catalogues which are not significantly contributing flux in a given PRIMAGER channel (e.g., quiescent galaxies). Figure 5 shows the percentage of sources which are above the point source sensitivity of the considered PRIMAGER survey for a given channel within the two Euclid-based prior catalogues. At the shortest wavelengths, less than 20% of sources present in the prior catalogues are actually significantly detectable (i.e., above the point source sensitivity) in the simulated maps themselves. The remaining sources will effectively be adding more complexity and degeneracy to the XID+ modelling. In order to mitigate this, as concluded by D24, some form of prior knowledge on the fluxes of the sources is required and is discussed in Section 3.3.

3.2.2. Blind source detection

PRIMA is scheduled to launch at a time where a plethora of ancillary data will be available, such as from Euclid (as described above), the Nancy Grace Roman space telescope, the Vera Rubin Observatory or radio surveys, such as from the Square Kilometre Array (SKA). Despite this, here we aim to demonstrate that PRIMAGER is capable of achieving its scientific goals in the absence of this data, in a fully self-contained way; detecting and analysing sources entirely from PRIMAGER observations. For this purpose, we perform a blind source detection.

In observations where source confusion is a significant contributor to the total map noise (σ_{total} ; $\sigma_{\text{total}}^2 = \sigma_{\text{inst}}^2 + \sigma_{\text{conf}}^2$), convolving with the PSF no longer optimises the signal-to-noise of isolated point sources. Instead, a matched (or Wiener) filter, created taking into account the noise properties of the map, is optimal

(Chapin et al. 2011). The blind detection process is outlined in D24, though a short summary is included here.

For each channel, a matched filter is created following the Chapin et al. (2011) prescription. Source detection is run on filtered maps using the `find_peaks` method provided by `photutils`. A source is determined to be present in a pixel if its value is the local maximum within a 5×5 pixel region centred on it. Maps are calibrated such that source flux can be estimated by directly reading the pixel value.

For confusion dominated channels, the application of the matched filter introduces distinct ringing features at known distances and intensities. These rings are likely to be detected as sources by the peak-finder algorithm if originating from sufficiently bright sources. To remove these false positives, we examine all sources which are expected to produce ringing features above σ_{total} . Peaks found in the expected ringing region, whose flux is less than five times the predicted ringing, are considered contaminated and are thus removed.

Similarly to D24, we cut the catalogue based on an observed flux threshold which corresponds to a 95% purity catalogue, where purity is defined as the fraction of detected peaks which have a counterpart in the true catalogue. The true counterpart is the brightest source which satisfies the following criteria: (i) the positional offset between the detected peak and the true source, d_{off} , satisfies $d_{\text{off}} \leq \text{FWHM}/2$, and (ii) the ratio of the observed and true flux, $S_{\text{obs}}/S_{\text{true}}$, satisfies $0.5 \leq S_{\text{obs}}/S_{\text{true}} \leq 2$.

This process is repeated for each channel, and the individual catalogues are merged to give a list of unique positional priors.

3.3. Flux priors

Within the XID+ framework, it is possible to utilise prior flux knowledge of specific sources to augment the performance of the modelling. This can be done by either using the prior flux knowledge to inform which sources will be kept in the prior source catalogue or by placing constraints on the source fluxes within the modelling itself.

The former was explored by Wang et al. (2024) whereby a neural network-based CIGALE emulator was used to predict Herschel/PACS and SPIRE fluxes from Spitzer/MIPS 24 μm photometry. These predicted fluxes then informed which sources were to be kept and passed to XID+. The actual modelling was then performed with uniform prior distributions on the fluxes for the remaining sources.

Another approach is to retain every source in the prior list and instead inform the prior distribution on the source fluxes within the modelling of XID+. D24 investigated this method by placing a Gaussian prior distribution on simulated source fluxes which were centred on the true flux of the given source and a standard deviation also equal to the true flux. This was designed to mimic a procedure which would utilise predicted FIR fluxes from SED-fitting data obtained at higher spatial-resolutions. D24 found that significant gains in flux modelling accuracy could be obtained when applying these flux priors for suitably high-density prior source catalogues, such as those based on Euclid data.

In the following we consider an extension of this method which fully utilises the hyperspectral imaging

capabilities of PRIMAgger to obtain prior flux information.

3.3.1. XID+stepwise

For the deep survey considered here, the first hyperspectral band of PRIMAgger, PHI1, will be instrumental noise limited due to the increased angular resolution at these shorter wavelengths significantly suppressing confusion noise. Therefore source flux measurements obtained across this band can be used to inform the prior flux constraints within the XID+ modelling at the confused longer wavelengths.

We propose a methodology (hereafter referred to as **XID+stepwise**) which steps through each PRIMAgger channel in ascending wavelength order (descending angular resolution) and performs the XID+ deblending with prior flux distributions constructed from the measured fluxes of the previous step. Specifically, the prior probability of the flux of source i , in a given channel j , is normally distributed around a mean μ with width σ :

$$p(S_{i,j}) \sim \mathcal{N}(\mu, \sigma). \quad (4)$$

The mean and the width are set to the same value which depends on the measured flux of the source from the previous, next-shortest wavelength channel, $S_{i,j-1}$, multiplied by some channel-dependent correction factor, C_j :

$$\mu = \sigma = C_j S_{i,j-1}. \quad (5)$$

The measured flux of the source at the previous channel, $S_{i,j-1}$, is taken as the median of the posterior for the given source from the previous XID+ fit. For the very first channel at 25 μm , the prior on the source fluxes is uniformly distributed between zero and the brightest pixel in the map. For all subsequent channels, the width of the prior is set to equal the mean in order to ensure it is wide enough to capture large changes in flux between bands due to, for example, the presence of PAH emission lines. This distribution is similarly truncated between zero and the brightest pixel in the map.

The wavelength-dependent correction factor takes into account the general change in SED between the observed wavelengths. It is determined by the average ratio between fluxes at a given wavelength and the previous wavelength for all galaxies within the SIDES simulation:

$$C_j = \frac{1}{N} \sum^N \frac{S_{i,j}}{S_{i,j-1}}, \quad (6)$$

which gives:

$$C_j = \begin{cases} 1.0; & j < 6 \text{ (PHI1)} \\ 1.3; & 6 \leq j < 12 \text{ (PHI2)} \\ 2.0; & j \geq 12 \text{ (PPI).} \end{cases} \quad (7)$$

On a source-by-source basis this correction factor has a large scatter and will also be redshift-dependent. However, here we conservatively consider a full population-based value as to minimally inform the SED variation between bands. This ensures that the method is not overly sensitive to the SED templates within the chosen simulation.

In addition, we will also consider the benefit of supplying some weak prior flux information at the first step, PHI1.1, and then applying the **XID+stepwise** methodology as outlined above. In these runs, we will adopt the toy flux prior model from D24, whereby the prior distribution on a source's flux in the PHI1.1 band is a Gaussian with a mean and width equal to the true flux of the source in this band. This will provide weak flux information at the initial step (as opposed to none in the regular **XID+stepwise** setup) which could be obtained from, for example, applying SED-fitting of ancillary optical/NIR photometry.

We perform three main runs in this work, summarised in Table 2. Our fiducial run consists of sources within the Euclid Wide positional prior and the newly introduced stepwise methodology, providing no flux information in the first band. Additionally, we run a Deep run, consisting of the Euclid Deep positional prior, and an informed stepwise flux prior. Finally, we perform a run which is purely PRIMAgger selected, with sources detected during blind source detection and a completely uninformed flux prior.

3.4. Systematic errors in the Point Response Function

To model how each source contributes flux to nearby pixels, XID+ estimates the PRF from an input PSF. Typically, we give XID+ the same PSF used to generate the maps. We expect to accurately measure the beam to within a few percent both prior to launch and in flight.

To quantify the impact of beam miscalibrations, we run XID+ on maps generated using the simplified Airy disc beams described in Section 2.4.2. The maps are kept the same for each run, varying only the model beam assumed by XID+. We perform four separate XID+ runs with beams derived from the Airy disc profile described in Eq. 2, comparing performance when providing XID+:

- (i) the true beam (i.e. the same beam used to generate the maps),
- (ii) a beam broadened by 5% ($r' = 1.05r$),
- (iii) a beam made elliptical by broadening one axis by 5% ($r' = \sqrt{(x/1.05)^2 + y^2}$), and
- (iv) a beam with 50% stronger ringing, implemented as

$$I'_0 = \begin{cases} I_0; & r < d_0 \\ 1.5I_0; & r \geq d_0, \end{cases} \quad (8)$$

where d_0 is the radius of the first Airy zero.

The results from this analysis is discussed in Section 4.3.

3.5. Modelling performance metrics

In order to quantify the flux accuracy of the XID+ modelling and to determine the level down to which we can reliably measure source fluxes from the PRIMAgger maps, we adopt the ‘limiting flux’ statistic of D24. It quantifies the deviation of the extracted fluxes, S_{obs} , from the true fluxes, S_{true} , within bins of true flux using the median absolute deviation, σ_{MAD} :

$$\sigma_{\text{MAD}}(S_{\text{true}}) = \alpha \cdot \text{Med} \left(\frac{\Delta S}{S_{\text{true}}} - \text{Med} \left(\frac{\Delta S}{S_{\text{true}}} \right) \right), \quad (9)$$

where $\Delta S = S_{\text{obs}} - S_{\text{true}}$ and $\alpha = 1.4826$ (which scales the MAD to a Gaussian). The limiting flux, S_{limiting} , is then defined as the flux at which σ_{MAD} equals 0.2:

TABLE 2
SPECIFICATIONS OF XID+ RUNS

Run Name	Positional Prior	Flux Prior	Source Density		
			PHI1_1	PHI2_1	PPI1
Fiducial	Euclid Wide	Stepwise (Uniform @ 25 μm)	0.11	0.37	0.91
Deep	Euclid Deep	Stepwise (Prior @ 25 μm)	0.31	1.00	2.47
Blind	Blind Detection	Uniform	0.05	0.16	0.39

NOTE. — A summary of the main runs included in this work. The positional prior specifies the locations at which XID+ should perform the deblending. Euclid Wide and Euclid Deep refer to the stellar mass-redshift cut achievable by the Euclid Wide and Deep Field surveys, respectively (Section 3.2.1). Blind refers to the source detection performed in a self-contained way (Section 3.2.2). Flux prior determines the prior flux information of individual sources given to XID+. Uniform uses a constant distribution limited to between zero and the brightest map pixel, whereas stepwise refers to the process of obtaining prior flux information for a given channel from the measurements made in the previous channel (Section 3.3.1). Source density refers to the number of sources present in the catalogue per beam, quoted for the PHI1_1, PHI2_1 and PPI1 channels (25, 47 and 92 μm).

$$S_{\text{limiting}} = S_{\text{true}} \Big|_{\sigma_{\text{MAD}}=0.2} . \quad (10)$$

This corresponds to the true flux at which the median deviation of the observed fluxes from the true values equals 20% of the true flux. Noise within the limiting flux statistic can arise due to the fact that it depends upon the binning of sources by their true flux values. As such, bootstrapping will be performed to estimate any uncertainty in the limiting flux.

4. RESULTS

4.1. Main results

Differences in our results from those in D24 arise primarily from the introduction of more realistic instrument parameters (beams, target sensitivity in noise model, etc.). For example, the sidelobe pattern has an impact in increasing the confusion noise. Nonetheless the overall performance remains similar, with the PHI1 channel being instrumental noise dominated, whilst confusion dominates from PHI2 onwards.

4.1.1. Fiducial run: using Euclid Wide priors

Our fiducial run started from the Euclid Wide prior source catalogue. We followed the XID+stepwise method described in Section 3.3.1, i.e. modelling the highest-angular resolution map at 25 μm without prior flux information and modelling the map of each subsequent channel with the prior flux information derived from the posterior of the previous channel, following Equations 4-7.

The output from XID+ is the full posterior distribution for the flux in the given channel for each source in the prior catalogue, including the correlation between sources. The flux of a source is quoted as the median of its marginalised posterior flux distribution. To limit the computational requirements, XID+ was applied to ~ 5 arcmin 2 tiles, and comprised 4 MCMC chains with 2000 warm-up and 2000 regular samples. For each tile posteriors for a background value and residual confusion noise are also obtained. These parameters capture flux from sources that may be missing from the prior catalogue or from any foreground contamination.

Using Equations 9 and 10, the limiting flux threshold, corresponding to a measured flux accuracy of 20% (5 σ), is determined for each of the PRIMAGER bands in the

fiducial run and are shown in Figure 6 and tabulated in Table 3. These are compared to the classical confusion limits, as calculated in Section 2.4, and the point source sensitivities of the simulated deep survey.

For all bands in PHI1 ($\lambda < 45 \mu\text{m}$), the instrumental noise dominates confusion and XID+ is able to recover accurate fluxes down to within 6–18% above the point source instrumental sensitivities. The the largest discrepancy is at PHI1_1. Even after accounting for noise via bootstrapping (shown by the blue shaded region in Figure 6), the limiting flux at PHI1_1 is still slightly above the point source sensitivity. This is due to the large number of sources in the prior catalogue. Many of these do not contribute significant flux to the map but do add degeneracy to the modelling (as shown in Figure 5), with flux from brighter sources misattributed to fainter sources. With only positional information and no prior flux information in this band to break the degeneracies, this results in a slightly elevated noise relative to the instrumental noise in the map. We return to this issue in Section 4.2.

For all channels in PHI2 and PPI ($\lambda \geq 45 \mu\text{m}$), confusion noise dominates the instrumental noise. The limiting flux of our fiducial run reaches below the classical confusion limit for all of these confusion-dominated channels. For PHI2, the limiting flux is a factor of 1.3–3.4 below the classical confusion limit between 45–84 μm . The biggest gains are achieved for PPI, where the limiting flux is factors of 4.5, 5.1, 4.2 and 3.0 below the confusion limits for PHI1 through PPI4 (92–235 μm), respectively.

In order to validate the robustness of the limiting flux statistic, we examine the distribution of the absolute relative errors between the observed and true fluxes for sources with an observed flux above the limiting flux. These are shown for all bands for our fiducial run in Figure 7. As can be seen, the median absolute relative error is well below the threshold of 0.2, representing an observed flux accuracy of 20%, for all bands. In fact, the typical (median) error is $\sim 6\%$. Moreover, the 84th percentile is also below 20% for all but the two longest wavelength bands.

There is however a bias of underestimating fluxes for faint sources and longer wavelength. This bias can be calibrated and thus corrected and is discussed in Appendix C. This underestimation is $\lesssim 5\%$ at the limiting flux for PHI1, increasing up to $\sim 15\%$ for PPI. The uncertainty

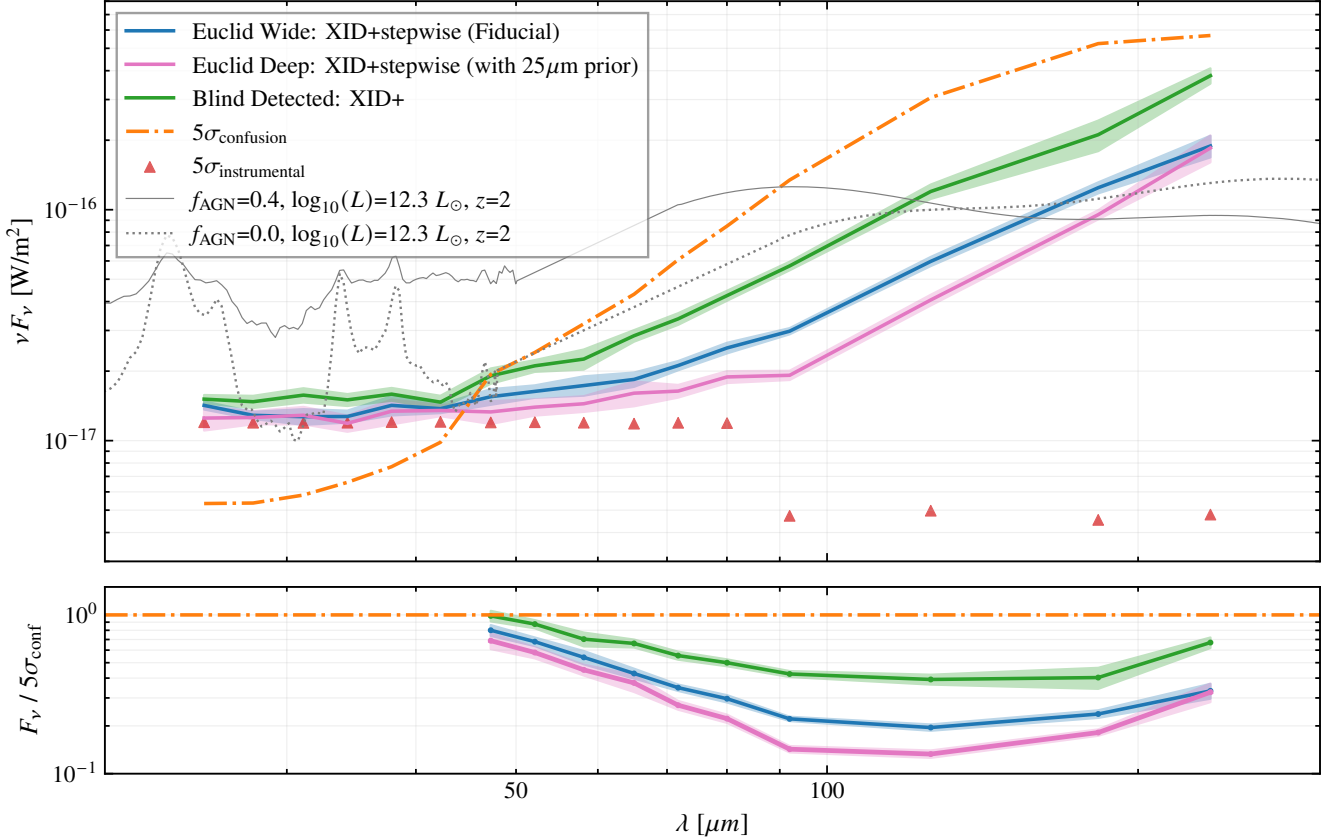


FIG. 6.— **Top:** Limiting flux density as a function of wavelength from 25–235 μm for **XID+** deblending of positional prior catalogues employing expected sensitivities for the Euclid Wide or Deep surveys. The instrumental sensitivities illustrated (red triangles) correspond to the anticipated sensitivities of the PRIMAGER Deep Survey. The confusion curve (dash-dot orange) illustrates the confusion noise computed for our expected beam and the SIDES sky model. The blue and magenta lines show the expected performance from our **XID+stepwise** model using Euclid prior catalogues with the anticipated sensitivities for the Wide and Deep fields respectively, with the shaded regions showing the 1σ uncertainty in this determination. For the Euclid Deep catalogue, a weak flux prior at 25 μm is supplied to reach the point source sensitivity. The limiting flux from **XID+** with no prior flux information for blind detected positional priors is also shown (green). The solid and dotted black curves show reference SEDs (Kirkpatrick et al. 2015) for two galaxies at $z = 2$ with L^* FIR luminosity (Magnelli et al. 2013), and AGN fractions of 0.4 and 0 respectively. The intersection between these curves and the blue and magenta lines show out to what PPI channel we expect to be able to recover fluxes. This shows that $z = 2$ L^* galaxies will be recovered out to channels 2 or 3 of PPI. **Bottom:** Limiting flux density reached by each run relative to the 5σ confusion limits for the 10 reddest channels which are confusion-dominated.

in the measured **XID+** fluxes, derived from the spread in their posterior distributions from **XID+**, are also discussed in Appendix C.

4.1.2. Using Euclid Deep priors

Figure 6 also shows the limiting flux reached when applying **XID+stepwise** to the Euclid Deep prior source catalogue along with some weak prior flux information at the first step, PHI1_1, as outlined at the end of Section 3.3.1. The high density of sources in the Euclid Deep catalogue (which contains ~ 2.8 times more sources than Euclid Wide) necessitates the use of prior flux information in the first step of **XID+stepwise** at PHI1_1 for the limiting flux to reach the point source sensitivity. This has a knock-on effect on the limiting flux depths in subsequent bands due to the **XID+stepwise** methodology. The very modest amount of prior flux information introduced at 25 μm leads to greater sensitivity in all wavelengths compared to the fiducial run, resulting in up to a factor of ~ 1.6 deeper limiting flux at PPI1, despite the larger number of catalogue sources. The Euclid Deep catalogue naturally has a significantly lower

fraction of sources which contribute significant flux to the maps across all the bands (as shown by Figure 5). Hence, without the additional flux information at the initial step, these extra sources would add degeneracies to the modelling and cause the limiting flux to lie above the point source sensitivity, an effect similar to that seen at PHI1_1 in our fiducial run. We further explore the impact of including and excluding prior flux knowledge for PHI1_1 in Section 4.2.

4.1.3. Using Blind priors

For our Blind run, we restrict ourselves to data obtainable by PRIMAGER, not utilising any ancillary data neither for positional nor flux priors. The positional prior arise from objects detected through matched filtering, and the flux prior is modelled in **XID+** with a uniform distribution. Even in this scenario, **XID+** is capable of reaching close to the instrumental noise for PHI1, averaging just 25% above the noise floor. Additionally, the limiting flux is up to a factor of 2 and 2.5 deeper than the confusion limit for PHI2 and PPI respectively.

TABLE 3
XID+ LIMITING FLUX

Channel	λ_{peak} [μm]	XID+stepwise: Euclid Wide Limiting Flux [μJy]	XID+stepwise: Euclid Deep Limiting Flux [μJy]	XID+: Blind Detection Limiting Flux [μJy]
PHI1_1	25.0	118 ± 5	104 ± 12	126 ± 5
PHI1_2	27.8	120 ± 4	117 ± 8	137 ± 8
PHI1_3	31.1	132 ± 10	134 ± 12	163 ± 12
PHI1_4	34.3	146 ± 9	136 ± 11	172 ± 10
PHI1_5	37.9	180 ± 17	170 ± 21	201 ± 13
PHI1_6	42.3	194 ± 8	190 ± 10	207 ± 13
PHI2_1	47.3	244 ± 19	210 ± 24	301 ± 23
PHI2_2	52.1	284 ± 17	243 ± 20	367 ± 21
PHI2_3	58.2	336 ± 32	280 ± 22	438 ± 43
PHI2_4	65.0	399 ± 28	348 ± 43	617 ± 35
PHI2_5	71.8	506 ± 23	393 ± 25	806 ± 46
PHI2_6	80.0	673 ± 35	504 ± 29	$1,130 \pm 56$
PPI1	92.0	914 ± 28	589 ± 27	$1,750 \pm 74$
PPI2	126	$2,510 \pm 110$	$1,710 \pm 90$	$5,040 \pm 360$
PPI3	183	$7,600 \pm 410$	$5,810 \pm 260$	$12,900 \pm 1,900$
PPI4	235	$14,800 \pm 1,600$	$14,500 \pm 1,900$	$29,800 \pm 2,200$

NOTE. — Limiting flux for each XID+ run in the 16 PRIMAGER channels, as presented in Figure 6. The channel name and central wavelength are given, with additional specifications for each channel presented in Table 1. The three runs are for the Euclid Wide catalogue with XID+stepwise (our fiducial run), the Euclid Deep catalogue with XID+stepwise (with a weak $25\mu\text{m}$ prior) and the blind detected catalogue with XID+ (summarised in Table 2). For each of the runs, the limiting flux is determined in each channel following Equations 9–10. Quoted errors are estimated from the RMS of bootstrapped samples.

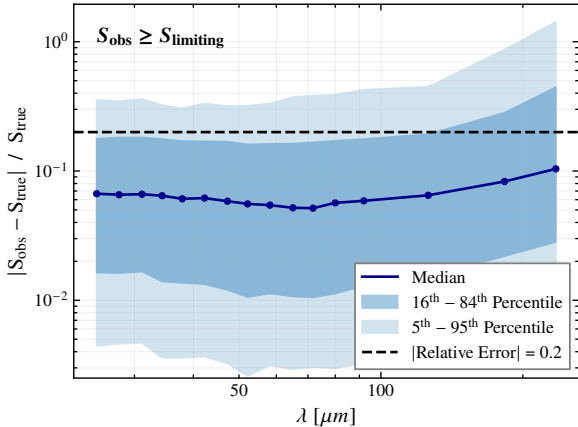


FIG. 7.— Distribution of the absolute relative errors between the observed and true fluxes from XID+stepwise for all sources with an observed flux above the limiting flux at the given wavelength for the Euclid Wide prior source catalogue. For all PRIMAGER bands, the median absolute relative error is well below the threshold of 0.2 (dashed black line) which represents an observed flux accuracy of 20%. The 84th percentile is also below this threshold for all but the two longest wavelength bands.

4.2. Improvement provided by XID+stepwise

In order to investigate the impact on recovered flux accuracy when applying prior flux knowledge via XID+stepwise, we also run XID+ without any flux information at any of the bands (i.e. with a uniform prior flux distribution from 0 to the brightest pixel value in the fitted region) for both Euclid positional prior catalogues.

For the Euclid Wide catalogue, we compare the limiting flux reached by XID+stepwise (i.e. our fiducial run) and that reached by the run with no prior flux information (referred to as the ‘uniform’ run) and show the

ratio between these two as the solid blue curve in Figure 8. At PHI1_1, this ratio is unity due to the first step in XID+stepwise assuming no prior flux information and applies the same uninformative, uniform distribution. For all subsequent bands, however, the limiting flux is improved by incorporating the flux information acquired from the previous band through XID+stepwise. For channels PHI1_2–PPI1, the limiting flux is improved by $\sim 5\text{--}15\%$, with even further improvements of $\sim 20\text{--}55\%$ for the most confused channels (PPI2–PPI4).

In all cases, but particularly for the high source density Euclid Deep catalogue, leveraging flux information acquired from the previous band through the stepwise methodology leads to substantial gains in the limiting flux. This is shown by the pink dashed curve in Figure 8, where the limiting flux reached in the confusion-dominated PHI2 channels (45–84 μm) using XID+stepwise are $\sim 20\text{--}40\%$ below that of running XID+. For the two longest (and most confused) wavelength bands, PPI3 and PPI4, this leads to very large gains, decreasing the limiting flux by $\sim 70\%$ relative to that of XID+.

It is worth noting the sharp peak seen at PPI1. This is due to a combination of the significantly better point source sensitivity in PPI (Figure 6), and a large increase in the number of sources within the prior source catalogue which significantly contribute flux to the map in this band (see Figure 5). This leads to good performance from XID+ in this channel and therefore less value is added from applying XID+stepwise.

We also investigate the impact of weak prior flux information at the first step of XID+stepwise, PHI1_1, as opposed to using an uninformative flat prior. This is motivated by the behaviour of the limiting flux relative to the point source sensitivity at PHI1_1 in our fiducial run as discussed in Section 4.1.1. Working with the Eu-

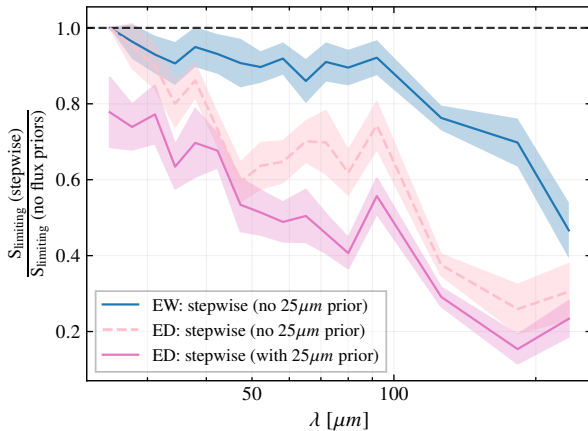


FIG. 8.— The ratios of the limiting flux reached by **XID+** when including (via the stepwise methodology) and excluding prior flux knowledge (where only a uniform flux prior distribution is used) for both Euclid catalogues. The ratios of the limiting fluxes of these runs are shown by the blue solid curve and pink dashed curve for the Euclid Wide and Deep catalogues, respectively. Significant gains in the limiting flux are achieved when applying **XID+stepwise** compared to the uniform run for both catalogues by up to a factor of four at the longest wavelengths. For the Deep catalogue, we also run **XID+stepwise** with a weak prior $25\text{ }\mu\text{m}$ flux for the PHI1_1 band. The ratio of the limiting flux from this run and that of the uniform run for the Deep catalogue is shown by the solid magenta curve. Comparing the solid magenta to the dashed pink curve highlights the additional gains at all wavelengths from supplying weak prior flux information at $25\text{ }\mu\text{m}$ for the Deep catalogue.

clid Deep catalogue, we obtain a $\sim 20\%$ improvement in the limiting flux depth is at PHI1_1 after applying a flux prior as outlined at the end of Section 3.3. This is illustrated by the first data point of the solid magenta curve in Figure 8. Application of this initial prior also consistently improves the limiting flux reached in the rest of the bands, compared with no prior flux information at $25\text{ }\mu\text{m}$.

For the Euclid Wide catalogue, however, supplying weak prior flux information at PHI1_1 has a negligible effect across all channels, except for PHI1_1 itself. This is due to the fact that the limiting flux is already very close to the point source sensitivities of PHI1 in the fiducial run, therefore the flux modelling is already performing as well as possible and is ultimately limited by instrumental sensitivity.

4.3. Variations from nominal

We investigate three systematic effects which may affect PRIMA observations: (i) the presence of cirrus, (ii) a telescope beam larger than currently expected, and (iii) the impact of miscalibration in the beam on **XID+** modelling.

We consider low, medium, and high levels of cirrus with corresponding intensities of 0.5, 1.5, and 2.5 MJy sr^{-1} respectively (see Sections 2.2.1 and 2.4.1). We also look at two scenarios where the telescope beam is broader than assumed: degraded and jittered (Section 2.4.2). Finally, we investigate the impact of our **XID+** model beam differing from the beam used to simulate the map, looking at a miscalibration in the width, ellipticity, and strength of sidelobes (Section 3.4). These runs are summarised in Table 4.

In all scenarios, we run **XID+** with the Euclid Wide

TABLE 4
SPECIFICATIONS OF VARIED RUNS

Variation Name	I_{100} [MJy sr $^{-1}$]	Map Beam	XID+ beam
Low Cirrus	0.5	Nominal	Nominal
Medium Cirrus	1.5	Nominal	Nominal
High Cirrus	2.5	Nominal	Nominal
Degraded	0.0	Degraded	Degraded
Jittering	0.0	Jittered	Jittered
Broader	0.0	Simplified	Broader
Elliptical	0.0	Simplified	Elliptical
Ringing	0.0	Simplified	Ringing

NOTE. — Summary of the different runs done to investigate the effects of systematics on our flux recovery. We consider low, medium, and high levels of cirrus contamination, corresponding to cirrus intensities (I_{100}) of 0.5, 1.5, and 2.5 MJy sr^{-1} respectively (Sections 2.2.1 and 2.4.1). We consider two scenarios, ‘degraded’ and ‘jittered’, where the telescope beam is broader than currently assumed (Section 2.4.2). Finally, we check perform three runs to see the effect of providing **XID+** with a beam that differs from the one used to create the maps, individually checking for the effect of beam width, ellipticity, and ringing strength (Section 3.4). All runs were performed with the Euclid Wide positional prior, and a uniform flux prior (i.e. not **XID+stepwise**).

positional prior, and a uniform flux prior (i.e. not **XID+stepwise**). Figure 9 shows the result of each of these runs.

For both the cirrus and beam-broadened scenarios, we provide **XID+** the same beam as was used to generate the maps, whereas we vary this for the miscalibration scenario.

For the cirrus-contaminated scenario, we run a larger area of the simulated field as the cirrus intensity varies significantly across the map. The presence of cirrus at the aforementioned intensities, representative of those expected at the anticipated locations of the PRIMAger deep fields, increases our limiting fluxes by, at worst, a factor of ~ 1.2 , ~ 1.4 , and ~ 1.9 respectively (Figure 9, upper panel). In any of these scenarios we expect to be able to recover accurate SEDs out to PPI2 using **XID+stepwise**, for the two reference SEDs shown in Figure 6.

The channels that are most affected are consistently PHI2_6, PPI1, and PPI2, with PPI3 and PPI4 being minimally affected. In the low cirrus scenario there is negligible impact on any of the PPI channels, whilst there is a noticeable impact on PHI2_6. The cirrus impact is a combination of the cirrus SED which peaks at $\sim 150\text{ }\mu\text{m}$, between PPI2 and PPI3, the power spectrum of the cirrus fluctuations and the local background estimator. Future work will explore their relative contributions. However, our results show that **XID+** applied to PRIMAger will perform well in the presence of expected cirrus levels.

In the beam-broadening scenario we compare the results of the broadened runs to those with our nominal beams (Figure 9, middle panel). Due to how both runs are parametrised, we would expect shorter wavelength (i.e. narrower beams) to be disproportionately affected. For the degraded beams, we find that our limiting flux increased by a factor of ~ 1.25 on average, peaking at ~ 1.5 in the PHI2_6 channel. With jittered beams, we instead find that the limiting flux increases by, at worst, $\sim 10\%$, averaging only a 2% increase over all channels.

Finally, for the beam calibration runs, we compare

them to a run where we gave XID+ the true map beam, the simplified beam described in Section 2.4.2. We find small yet persistent improvements to our limiting flux for PHI1, although they are consistent with no change to within one sigma (Figure 9, lower panel). Where we overestimate the beam width, we find that our limiting fluxes are, at worst, a factor of ~ 1.18 higher at PPI3, and averaging ~ 1.07 for PHI2 and PPI. A slightly elliptical beam follows a similar relation, though roughly half as impactful, peaking at ~ 1.09 , again at PPI3, and averaging ~ 1.03 for PHI2 and PPI. Finally, even with a miscalibration of the beam of sidelobes 50% stronger than nominal, our limiting fluxes are at worst a factor of ~ 1.06 higher, averaging ~ 1.02 for PHI2 and PPI. This is as expected since the majority of the power of the beam lies within the central lobe. We expect the PRIMAgger beam to be calibrated to higher precision than the variations considered here, so we are confident that XID+ is resilient to realistic miscalibrated beam inputs.

5. DISCUSSION

Our results have shown that accurate flux measurements can be obtained well below the confusion limits of all the confusion-dominated PRIMAgger channels. This is achieved for sources detected in deep optical/NIR observations from both the Euclid Wide and Deep field surveys and self-consistently with blindly detected sources. Here we discuss the implications of our results for a specific science case as well as the limitations and requirements for future improvement of our work.

5.1. IR-luminous galaxies at cosmic noon

In order to further evaluate the performance of our fiducial run, we look at the specific science case of IR-luminous galaxies at cosmic noon ($z \sim 2$). These sources are of particular interest due to significant fractions of their star formation being dust-obscured and are observed at an epoch where cosmic star formation peaked. Specifically, we look at sources within the simulated survey area which have $1.9 \leq z \leq 2.1$ and an IR luminosity greater than the characteristic luminosity at this redshift, $L_{\text{IR}}^* = 10^{12.3} L_{\odot}$ (Magnelli et al. 2013). As these sources have $L_{\text{IR}} > 10^{12} L_{\odot}$, we refer to them as ultra-luminous IR galaxies (ULIRGs).

In Figure 6, we show the model SEDs of two such sources from Kirkpatrick et al. (2015), both of which have an L_{IR}^* luminosity at $z = 2$ but with differing AGN fractions, relative to the limiting fluxes reached by our three main runs. A key science case of PRIMA will be to recover the SEDs of such sources in order to determine their physical parameters. Bisigello et al. (2024) and Boquien et al. (2025) demonstrated that this is achievable if accurate flux measurements are obtained up to and including the PPI2 channel. As shown in Figure 6, this is accomplished by our fiducial run as well as our Euclid Deep run since the limiting flux curves are well below the flux of these two model SEDs. For the blind detected run, however, the limiting flux lies just slightly above the two SEDs in PPI2, implying that their photometry will be recovered at a significance slightly lower than 5σ in that scenario.

Similarly to Figure 7, we show in Figure 10 the distribution of the absolute relative errors between the observed and true fluxes of these $z = 2$ ULIRGs which have

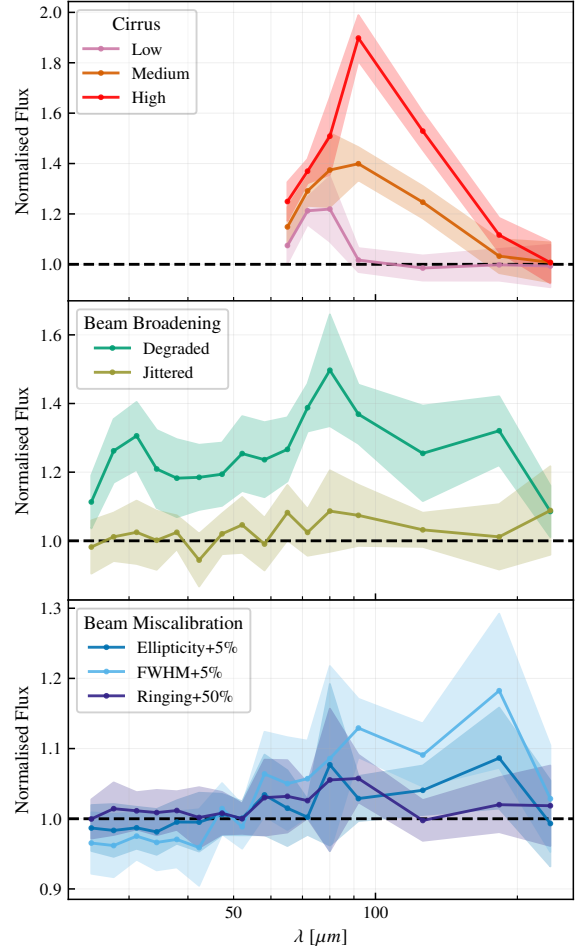


FIG. 9.— Impact of various systematics on the modelling accuracy of XID+ across the PRIMAgger bands. **Top:** Limiting flux achieved by XID+ in the presence of simulated galactic cirrus, normalised by the limiting flux of our fiducial run (dashed black line). We consider cirrus of varying intensities ($0.5, 1.5$, and 2.5 MJy sr^{-1}) which are representative of the extragalactic fields PRIMAgger is likely to observe. Uncertainties are estimated via bootstrapping. **Middle:** The impact of broadening the beam of the map on which XID+ is run. This broadening could result from a smaller telescope aperture or some worsening of the optics (shown by the Degraded beams curve). It could also result from the positional offsets of target sources from jittering, requiring a stacking of sky scans leading to a blurring effect (shown by the Jittered curve). **Bottom:** The impact of supplying XID+ with a beam which differs from the true beam of the map. These represent potential miscalibrations in the beam’s ellipticity, FWHM or ring features.

an observed flux greater than the limiting flux from our fiducial run. Due to the lower number of sources in this narrow z slice, this distribution is naturally more noisy than that for the full fiducial run. However, it is evident that the observed fluxes for these sources are accurate, with the median absolute relative error being well below the 0.2 threshold, corresponding to a flux accuracy of 20% of the true flux. Moreover, the 84th percentile is

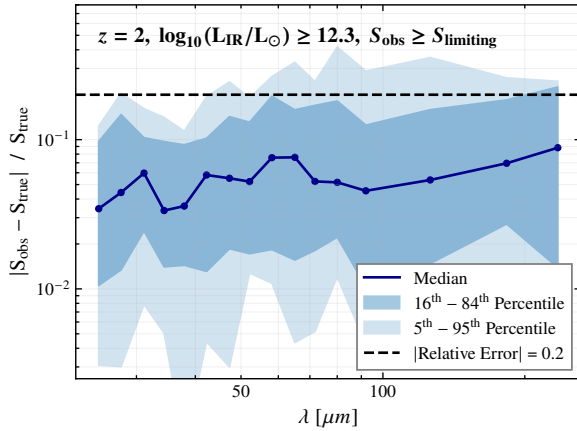


FIG. 10.— Distribution of the absolute relative errors between the observed and true fluxes from the fiducial run for sources at $z=2$ and with $\text{LIR} \geq 10^{12.3} \text{ L}_\odot$ and an observed flux above the limiting flux.

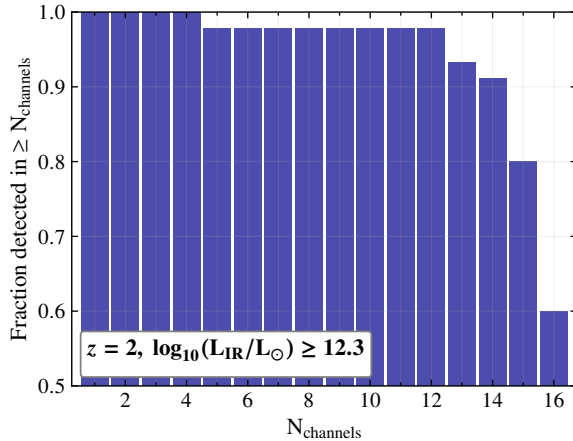


FIG. 11.— Cumulative histogram showing the fraction of $z=2$, $\text{LIR} \geq 10^{12.3} \text{ L}_\odot$ sources which are detected in a minimum number of channels. A source is considered detected if it has an observed flux greater than the limiting flux in a given band. All of the $z=2$, ULIRGs in the simulated survey are detected in at least four channels, with 60% having detections in all channels. Nearly all ($\sim 98\%$) are detected in at least 12 of the PRIMAgger channels, providing robust sampling of the SEDs of these scientifically interesting sources.

below this threshold for all but the longest wavelength channel, PHI1.

Additionally, the impact of PAH emission is evident in the median absolute relative error, which drops for the PHI1_4 and PHI1_5 channels. At this redshift, these channels cover the $11.3 \text{ }\mu\text{m}$ and $12.7 \text{ }\mu\text{m}$ PAH spectral features, which in turn raise the flux of these sources relative to the point source sensitivity. This elevated signal-to-noise is then naturally reflected in the improved flux modelling accuracy.

If we again only consider sources with an observed flux above the limiting flux from our fiducial run as being detected within a given band, we can determine the completeness of our fiducial run for the $z=2$ ULIRGs. In Figure 11, we show the cumulative fraction of these sources which are detected in a given number of the

representative PRIMAgger channels. As shown, all of these sources are detected in at least 4 channels and $\sim 98\%$ of them have detections in at least 12 channels. Moreover, 60% of the $z=2$ ULIRGs within the simulated survey area have detections in all channels. As such, our fiducial run is capable of providing robust sampling of the SEDs of these sources across the FIR wavelength range probed by PRIMAgger.

This is further demonstrated in Figure 12, which highlights the capability of XID+stepwise in extracting accurate flux measurements for these sources from confusion-dominated maps. We show the measured photometry from our fiducial run relative to the true SEDs for two ULIRGs at cosmic noon. The first, denoted as source A, is an isolated source relative to the size of the beam at PHI1 (which the resolution of the RGB image has been degraded to). As such, the measured photometry for this source is within 7% of the true flux at all of the PRIMAgger channels. The second source (denoted as source C), however, has two close neighbours which reside at lower redshifts, as shown by the bottom zoom inset of the RGB image in Figure 12, depicting the PHI1_1 intensity map at the location of these sources. At the angular resolution of PHI1, these three sources are completely blended together. As such, they significantly benefit from the utilisation of flux information obtained from the higher resolution maps in which they are not blended (i.e. via XID+stepwise). This leads to all the recovered fluxes of source C being within 14% for all channels except for PHI1_1, which has a measured flux 30% the true value.

5.2. Future Work

Future work will look to further develop the simulated PRIMAgger map generation as well as the modelling within XID+. For the former, there are several aspects which can be improved. First, our model of the extragalactic sky, the SIDES simulation, does not include AGN. Recently, however, Vidal et al. (2025) presented updates to the SIDES simulation which include modified star-forming and starburst SED templates as well as quiescent and AGN templates. Second, including simulated zodiacal emission in addition to galactic cirrus would further ensure that the performance of XID+stepwise is robust to foreground contamination. Third, realistic simulated instrumental noise will need to be incorporated which includes, for example, the spatial correlations from the telescope beam, $1/f$ noise and effects from scanning strategies. These are currently being developed as part of a realistic simulated map-maker for PRIMAgger and will therefore be used in any future work testing flux recovery with XID+.

With regards to XID+, extending the modelling of the noise parameters to include the covariance from confusion noise will significantly improve the overall flux modelling, particularly in terms of the spread of the source flux posteriors (and therefore the quoted errors on the photometry). Additionally, we will look to improve the modelling of the background and thereby resolve the underestimation of faint source fluxes, as described in Appendix C.

It is also possible to incorporate even tighter prior flux constraints within the XID+stepwise framework by utilising all the spectral filters within the two PHI bands. In this work, we only considered using a combination of

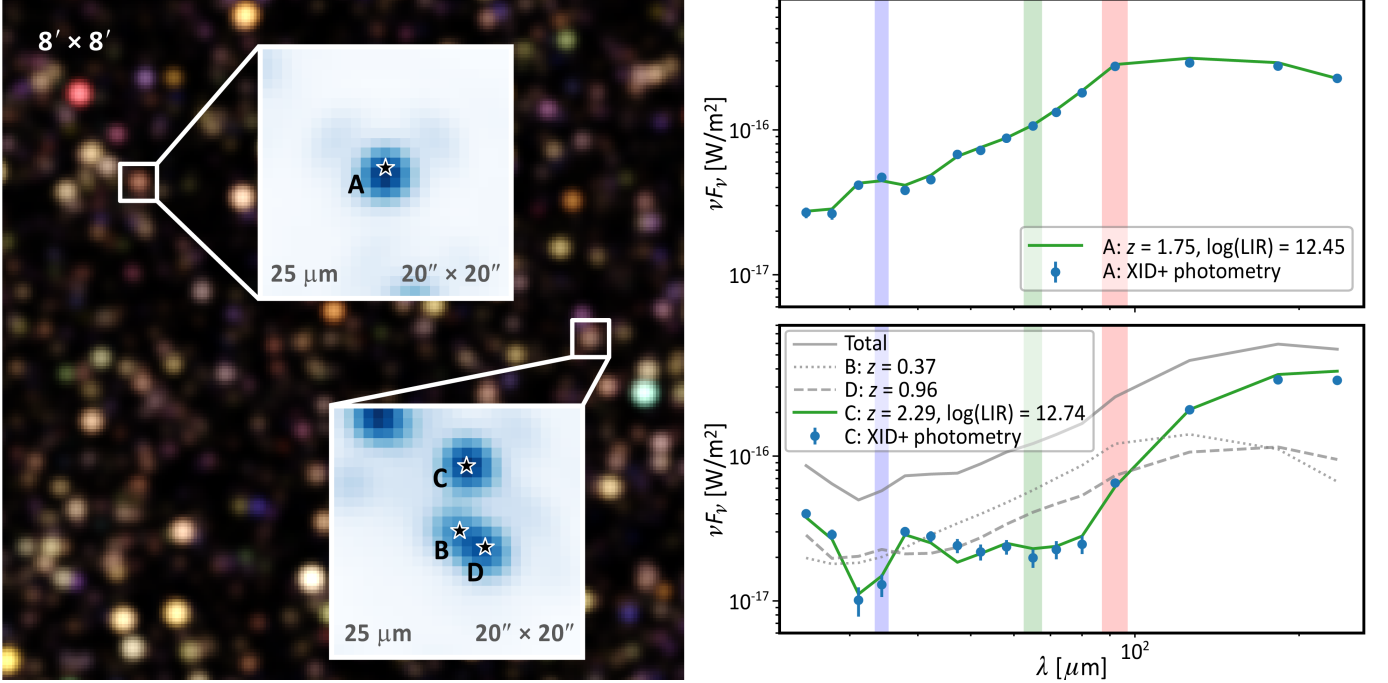


FIG. 12.— Demonstration of the deblending capabilities of **XID+stepwise**. **Left:** RGB cutout of the simulated PRIMAgger map where blue, green and red correspond to the PHI1_4, PHI2_4 and PPI1 channels, respectively, with the resolution of each band degraded to that of PPI1. Also shown are insets of two regions of the PHI1_1 map which contain an IR-luminous source with a redshift near cosmic noon. The top inset shows one of these sources (source A) which is relatively isolated, whilst the bottom shows another (source C) which has two close neighbours in the projected plane, but are at lower redshifts (sources B and D). As can be seen in the RGB image, sources B, C and D are blended together at the resolution of PPI1. **Right:** Recovered SEDs of the cosmic noon, IR-luminous sources A and C from **XID+stepwise** photometry relative to their true SEDs from the SIDES simulation.

the available PHI filters. Using all of them, however, allows for finer steps between wavelengths and thereby making the prior flux constraint obtained from one filter more accurate for the next filter. An extension to **XID+stepwise** could also possibly fit the SEDs of the sources by constraining against the maps from all channels simultaneously.

It is worth noting that other techniques for obtaining fluxes below the confusion limit are also possible, such as utilising auto-encoders and deep learning methods to super-resolve the confusion-dominated maps. Lauritsen et al. (2021) and Koopmans et al. submitted demonstrated such techniques for Herschel/SPIRE 500 μ m maps. A future paper will explore deep learning based super-resolution methods on de-confusion in the context of PRIMAgger.

6. CONCLUSIONS

In this work, we have demonstrated that accurate flux measurements can be obtained well below the confusion limits for all confusion-dominated PRIMAgger channels. By leveraging PRIMAgger’s hyperspectral capabilities, informative flux priors can be constructed by stepping through the spectral channels sequentially. For Euclid-based positional prior catalogues, we have shown that the short-wavelength, higher angular resolution PRIMAgger data can be used to successfully deblend sources below the confusion limits in the longest wavelength PRIMAgger maps.

We have tested these methods on mock data that simulate a deep 1500 hr deg $^{-2}$ imaging survey with PRIMAgger, from 25–235 μ m. These have been updated from D24 to reflect the latest PRIMAgger instrument specifici-

cations. As such, they have been generated using a sky, observatory, and instrument characteristics that provides maps with realistic confusion and instrumental noise.

For our fiducial run, we have shown that for a positional prior catalogue with the anticipated sensitivity of the Euclid Wide Field survey, our **XID+stepwise** methodology recovers accurate photometry of source fluxes (to within 20%) which are a factor of 1.3–3.4 below the confusion limits between 45–84 μ m. Further gains were achieved for the most confused maps in the PPI channels (92–235 μ m), with accurate flux measurements obtained at factors of \sim 3–5 below the confusion limit.

For the Euclid Deep positional prior catalogue, we found that weak prior flux information is required at PHI1_1 (25 μ m) in addition to our **XID+stepwise** model in order to accurately recover fluxes down to the point source sensitivities of the PHI1 channels. By doing so, we showed that even further gains below the confusion limits are achieved relative to our fiducial run for all confusion-dominated channels, with up to a factor \sim 1.6 deeper limiting flux at PPI1 (92 μ m).

By conducting blind source detection through matched-filtering of the PRIMAgger maps, we also showed that accurate flux measurements from **XID+** below the confusion limits are currently achievable using data from PRIMAgger in a self-contained way. We have therefore demonstrated that imaging data from PRIMAgger will not be limited by naïve, classical confusion noise if deblending with **XID+** is employed, with further gains possible from Euclid-like positional priors and **XID+stepwise**.

From these results, we showed that accurate flux measurements were obtained with high spectral sampling from PRIMAgger for $z = 2$, IR-luminous sources. For

those with an IR luminosity greater than the characteristic luminosity at $z = 2$, 60% are detected in all 16 PRIMAger channels, spanning 25–235 μm . Moreover, nearly all ($\sim 98\%$) are detected in at least 12 of the channels, thereby providing robust sampling of the FIR-regime of the SEDs of these dust-obscured, star-forming galaxies residing at the epoch of peak star-formation.

We demonstrated that these results are robust to various systematic effects such as galactic cirrus, degraded optics and various miscalibration effects.

AUTHOR CONTRIBUTIONS

The contributions of the authors using the Contributor Roles Taxonomy (CRediT) were as follows. **James Donnellan:** Methodology, Software, Validation, Investigation, Writing - original Draft **Borja Pautasso:** Methodology, Software, Validation, Investigation, Writing - original Draft **Seb Oliver:** Conceptualization, Supervision, Project Administration, Writing - Review & Editing, Funding acquisition **Matthieu Bethermin:** Resources, Conceptualization, Writing - Review & Editing **Longji Bing:** Methodology, Software, Validation, Investigation **Alberto Bolatto:** Conceptualization,

Writing - Review & Editing **Laure Ciesla:** Conceptualization, Writing - Review & Editing **Dennis Koopmans:** Writing - Review & Editing **Alex Pope:** Conceptualization, Writing - Review & Editing **Stephen Serjeant:** Cirrus, writing - Review & Editing **Lingyu Wang:** Writing - Review & Editing

ACKNOWLEDGEMENTS

We thank David Leisawitz and Alexander Kashlinsky (NASA Goddard) for helpful discussions on the topic of modelling cirrus, and Darren Dowell (NASA JPL) and Willem Jellema (SRON) for providing details and discussion on the beams. We also thank John Arballo (NASA JPL) for help with the formatting of Figure 12. JMSD, BP and SJO acknowledge funding from the UK Space Agency under grant UKRI3191. JMSD was supported by the Science and Technology Facilities Council, grant number ST/W006839/1, through the DISCnet Centre for Doctoral Training. AB, AP and JDS acknowledge funding for the PRIMA Phase A study from NASA.

DATA AVAILABILITY STATEMENT

All data will be made available upon acceptance for publication.

REFERENCES

Barchiesi L., et al., 2025, *JATIS*, 11, 031609
 Béthermin M., et al., 2017, *A&A*, 607, A89
 Béthermin M., et al., 2022, *A&A*, 667, A156
 Béthermin M., et al., 2024, *A&A*, 692, A52
 Bisigello L., et al., 2024, *A&A*, 689, A125
 Boquien M., Ciesla L., Amestoy R., Glenn J., Gruppioni C., Smith J.-D., 2025, *JATIS*, 11, 031619
 Bradford C. M. M., et al., 2025, *JATIS*, 11, 031627
 Burgarella D., Bethermin M., Boselli A., Donnelan J. S., Dowell C. D., Lagache G., Oliver S., Dole H., 2025, *JATIS*, 11, 031639
 Calzetti D., Armus L., Bohlin R. C., Kinney A. L., Koornneef J., Storchi-Bergmann T., 2000, *ApJ*, 533, 682
 Cardelli J. A., Clayton G. C., Mathis J. S., 1989, *ApJ*, 345, 245
 Casey C. M., 2012, *MNRAS*, 425, 3094
 Casey C. M., Narayanan D., Cooray A., 2014, *Phys. Rep.*, 541, 45
 Chapin E. L., et al., 2011, *MNRAS*, 411, 505
 Ciesla L., et al., 2025, *JATIS*, 11, 031625
 Condon J. J., 1974, *ApJ*, 188, 279
 Conroy C., 2013, *ARA&A*, 51, 393
 Dole H., et al., 2006, *A&A*, 451, 417
 Donnan F. R., Rigopoulou D., García-Bernete I., Bisigello L., Aalto S., 2025, *JATIS*, 11, 031606
 Donnelan J. M. S., et al., 2024, *MNRAS*, 532, 1966
 Draine B. T., 2003, *ARA&A*, 41, 241
 Draine B. T., 2011, Physics of the Interstellar and Intergalactic Medium
 Dunlop J. S., et al., 2017, *MNRAS*, 466, 861
 Euclid Collaboration: Aussel H., et al., 2025, *arXiv e-prints*, p. arXiv:2503.15302
 Euclid Collaboration: Enia A., et al., 2025, *arXiv e-prints*, p. arXiv:2503.15314
 Euclid Collaboration: Scaramella R., et al., 2022, *A&A*, 662, A112
 Euclid Collaboration: Tucci M., et al., 2025, *arXiv e-prints*, p. arXiv:2503.15306
 Faisst A. L., Chen C.-C., Ciesla L., Gruppioni C., 2025, *JATIS*, 11, 031630
 Farrah D., et al., 2025, *arXiv e-prints*, p. arXiv:2511.13849
 Fernández-Ontiveros J. A., Spinoglio L., Nagao T., 2025, *JATIS*, 11, 031637
 Fudamoto Y., et al., 2020, *A&A*, 643, A4
 Gautier III T. N., Boulanger F., Perault M., Puget J. L., 1992, *AJ*, 103, 1313
 Gkogkou A., et al., 2023, *A&A*, 670, A16
 Glenn J., et al., 2025, *JATIS*, 11, 031628
 Gruppioni C., et al., 2020, *A&A*, 643, A8
 Hauser M. G., Dwek E., 2001, *ARA&A*, 39, 249
 Hauser M. G., et al., 1998, *ApJ*, 508, 25
 Hurley P. D., et al., 2017, *MNRAS*, 464, 885
 Inami H., et al., 2022, *MNRAS*, 515, 3126
 Ishiyama T., et al., 2021, *MNRAS*, 506, 4210
 Jellema W., et al., 2024, in Zmuidzinas J., Gao J.-R., eds, SPIE Conference Proceedings Vol. PC13102, Millimeter, Submillimeter, and Far-Infrared Detectors and Instrumentation for Astronomy XII. SPIE, doi:10.1117/12.3020634
 Kennicutt Jr. R. C., 1998, *ARA&A*, 36, 189
 Kirkpatrick A., Pope A., Sajina A., Roebuck E., Yan L., Armus L., Díaz-Santos T., Stierwalt S., 2015, *ApJ*, 814, 9
 Klypin A., Yepes G., Gottlöber S., Prada F., Heß S., 2016, *MNRAS*, 457, 4340
 Laureijs R., et al., 2011, *arXiv e-prints*, p. arXiv:1110.3193
 Lauritsen L., Dickinson H., Bromley J., Serjeant S., Lim C.-F., Gao Z.-K., Wang W.-H., 2021, *MNRAS*, 507, 1546
 Leinert C., et al., 1998, *A&AS*, 127, 1
 Li A., 2020, *Nature Astronomy*, 4, 339
 Low F. J., et al., 1984, *ApJ*, 278, L19
 Madau P., Dickinson M., 2014, *ARA&A*, 52, 415
 Magnelli B., et al., 2013, *A&A*, 553, A132
 Miville-Deschénes M.-A., Lagache G., 2005, *ApJS*, 157, 302
 Miville-Deschénes M.-A., Lagache G., Boulanger F., Puget J.-L., 2007, *A&A*, 469, 595
 Mouillet A., et al., 2023, *arXiv e-prints*, p. arXiv:2310.20572
 Mouillet A., et al., 2025, *arXiv e-prints*, p. arXiv:2511.10927
 Mullaney J. R., Alexander D. M., Goulding A. D., Hickox R. C., 2011, *MNRAS*, 414, 1082
 Nguyen H. T., et al., 2010, *A&A*, 518, L5
 Pearson W. J., Wang L., van der Tak F. F. S., Hurley P. D., Burgarella D., Oliver S. J., 2017, *A&A*, 603, A102
 Pearson W. J., et al., 2018, *A&A*, 615, A146
 Pope A., et al., 2008, *ApJ*, 675, 1171
 Puget J. L., Abergel A., Bernard J. P., Boulanger F., Burton W. B., Desert F. X., Hartmann D., 1996, *A&A*, 308, L5
 Rodríguez-Puebla A., Behroozi P., Primack J., Klypin A., Lee C., Hellinger D., 2016, *MNRAS*, 462, 893
 Salim S., Narayanan D., 2020, *ARA&A*, 58, 529
 Shirley R., et al., 2019, *MNRAS*, 490, 634
 Shirley R., et al., 2021, *MNRAS*, 507, 129
 Shvai I., et al., 2024, *A&A*, 690, A89
 Traina A., et al., 2025, *JATIS*, 11, 031631
 Valiante E., et al., 2016, *MNRAS*, 462, 3146
 Vidal E. P., et al., 2025, *arXiv e-prints*, p. arXiv:2509.15331

Walcher J., Groves B., Budavári T., Dale D., 2011, *Ap&SS*, **331**, 1
 Wang L., et al., 2021, *A&A*, **648**, A8
 Wang L., et al., 2024, *A&A*, **688**, A20

Yoon I., et al., 2025, *JATIS*, **11**, 031634
 Zavala J. A., et al., 2021, *ApJ*, **909**, 165
 Zubko V., Dwek E., Arendt R. G., 2004, *ApJS*, **152**, 211

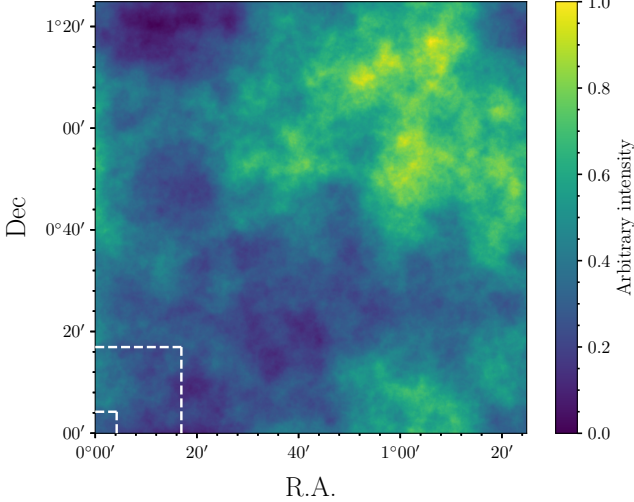


FIG. A1.— Structure of simulated cirrus over the entire 2 deg² produced by the fBm process. The structure map is in arbitrary units. The larger and smaller bounded areas correspond to the cutouts presented in Figures 3 and 2 respectively.

APPENDIX

A. CIRRUS STRUCTURE

Fractional Brownian motion is characterised by one parameter, the Hurst exponent (H), which determines the correlation between successive changes. When H is 0.5 the field is uncorrelated, whereas values above or below this indicate a positive or negative correlation respectively. For our work, we use $H = 0.7$. The output of the fBm process is shown in Figure A1.

We first create the structure map with map pixels of 0''.1, and downscale to the PRIMAGER pixel sizes. After convolving the map with the beam, we measure the RMS via a double aperture chopping method as described in Gautier et al. (1992). We normalise our maps to get the correct RMS, as predicted by Gautier et al. (1992) and Miville-Deschénes et al. (2007). Although this will give us the correct variance at the scale of aperture, at other scales, both larger and smaller, this is likely to not be the case. With the Miville-Deschénes et al. (2007) correction, the emission intensity scales linearly with I_{100} . Finally, we scale from the reference 100 μm to the desired wavelength by utilising the interstellar dust SED from Zubko et al. (2004).

Before running XID+ on the cirrus-contaminated maps, we first perform a local background subtraction process. It estimates the background by first applying a 3σ clipped median filter across the map, and a boxcar filter afterwards to smooth it out.

Future work will look at the variance of the structure map at differing scales, alongside different subtraction algorithms.

B. PRIMAGER BEAMS

Figure B1 shows the 2D and radial profile of three representative PRIMAGER channels: PHI1_1, PHI2_1, and

PPI1. The logarithmic view in the top panel shows the various effects introduced by including more realistic optical simulations. The bottom panel shows the radial profile of both the nominal and simplified beams (Section 2.4.2) after accounting for the map pixels.

C. XID+ BIASES

Figure C1 looks at the distribution of relative errors between the observed and true fluxes from our fiducial run as a function of the true flux of the sources. These highlight a systematic underestimation in flux from XID+ which becomes more pronounced for fainter sources and as the observed wavelength increases (and angular resolution decreases). This arises due to a degeneracy between the background parameter and the residual confusion noise parameter within the modelling of XID+ (Equation 3). A solution with an elevated background value can be found either when bright sources are missing in the prior catalogue, or from bright sources being cut off at the edge of a tile during the tiling procedure. Subsequently, extra flux is then present in the map which can't be accounted for by the known sources in the model, as these may be too far from the regions of this unaccounted-for flux (as per the PRF). This forces the background parameter to increase. Since this background is also assumed to be constant across the tile, then the background will be too high in other areas and thus lead to a reduction in the fluxes of the known sources.

If this background parameter, which is a free parameter, is instead set to a constant value determined empirically to be the correct value, then this underestimation in the fluxes disappears. Additionally, the residual confusion noise parameter increases to compensate. Future work will investigate applying a non-uniform background model in order to resolve this issue.

We also look at the accuracy of the errorbars on the fluxes measured by XID+ in our fiducial run. These are taken as the maximum between the 16th-50th percentile and the 50th-84th percentile of the posterior samples for a given source from the MCMC fit within XID+. This gives the 1σ error in the measured flux of a source, which is taken as the median of the samples. The accuracy of these errors can be checked by seeing how far away the true flux value of the source (S_{true}) is from the measured flux (S_{obs}), normalised by the error in the flux measurement ($\sigma_{\text{posterior}}$). Ideally, this would correspond to the standard Gaussian distribution, whereby S_{true} will be within $1\sigma_{\text{posterior}}$ of S_{obs} for 68% of the sources.

As such, in Figure C2 we plot the histograms of these values for sources within our fiducial run which have an observed flux above the limiting flux in a given channel. For the PHI1 channels, these histograms do indeed match the expected standard Gaussian. However, for the PHI2 and PPI channels, they move away from the standard Gaussian and become ever more biased towards negative values. This is due to the bias in XID+ to underestimate the flux, as discussed above and shown in Figure C1. What is also evident is the increase in the spread of the histograms relative to the standard Gaussian for these channels. This indicates that the

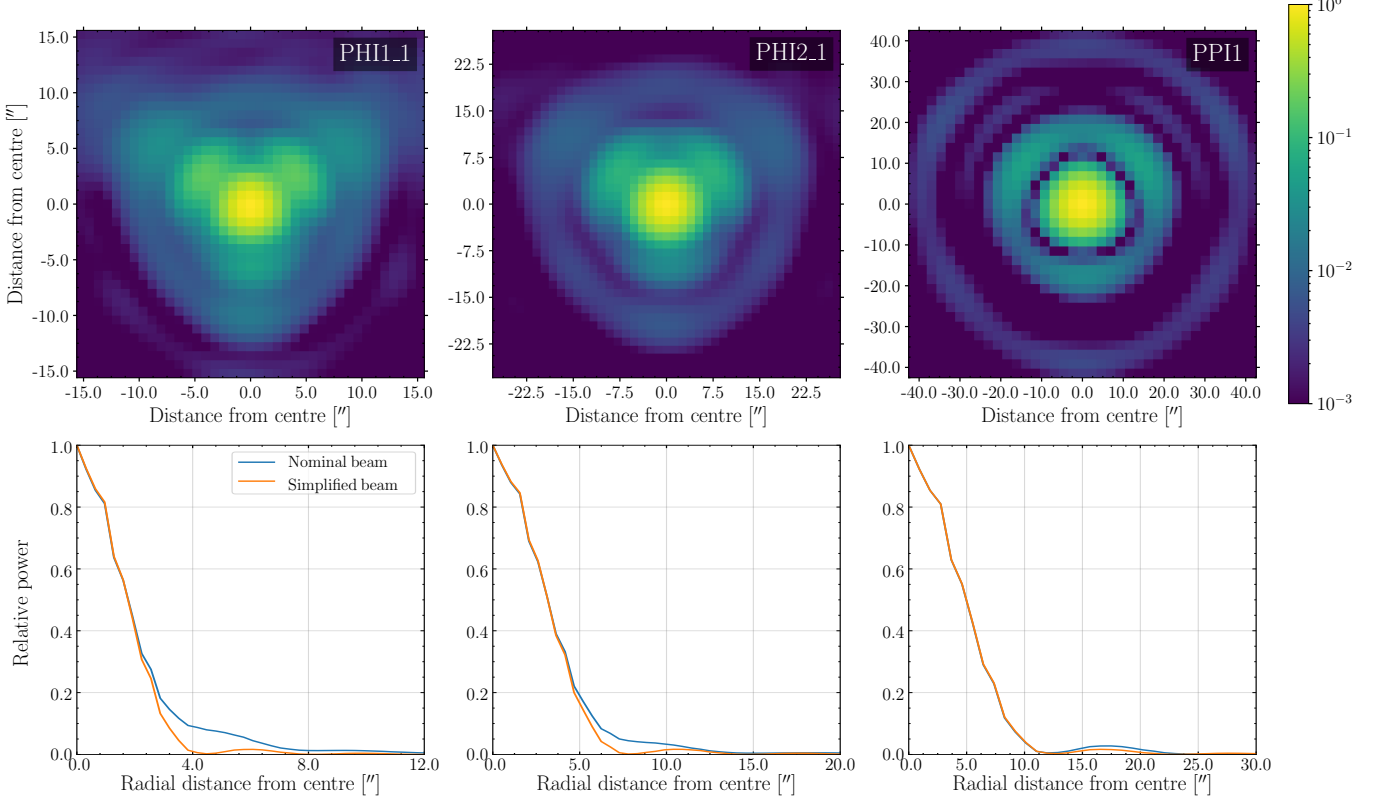


FIG. B1.— 2D logarithmic view of beam PSF (top) and radial profile (bottom) for PHI1_1, PHI2_1, and PPI1. **Top:** 2D logarithmic view of the beam PSF for PHI1_1, PHI2_1, and PPI1. The various optical features present are apparent. **Bottom:** Radial profile of the nominal and simplified beam (Section 2.4.2) after accounting for map pixelisation.

errors on the measured fluxes (i.e. the spread in the flux posteriors) become increasingly underestimated as the wavelength increases. This is due to the residual confusion noise parameter within the XID+ model (Equation 3) not taking into account the correlations between pixels. Future work will look to account for this covariance within the modelling.

This paper was built using the Open Journal of Astrophysics L^AT_EX template. The OJA is a journal which provides fast and easy peer review for new papers in the `astro-ph` section of the arXiv, making the reviewing process simpler for authors and referees alike. Learn more at <http://astro.theoj.org>.

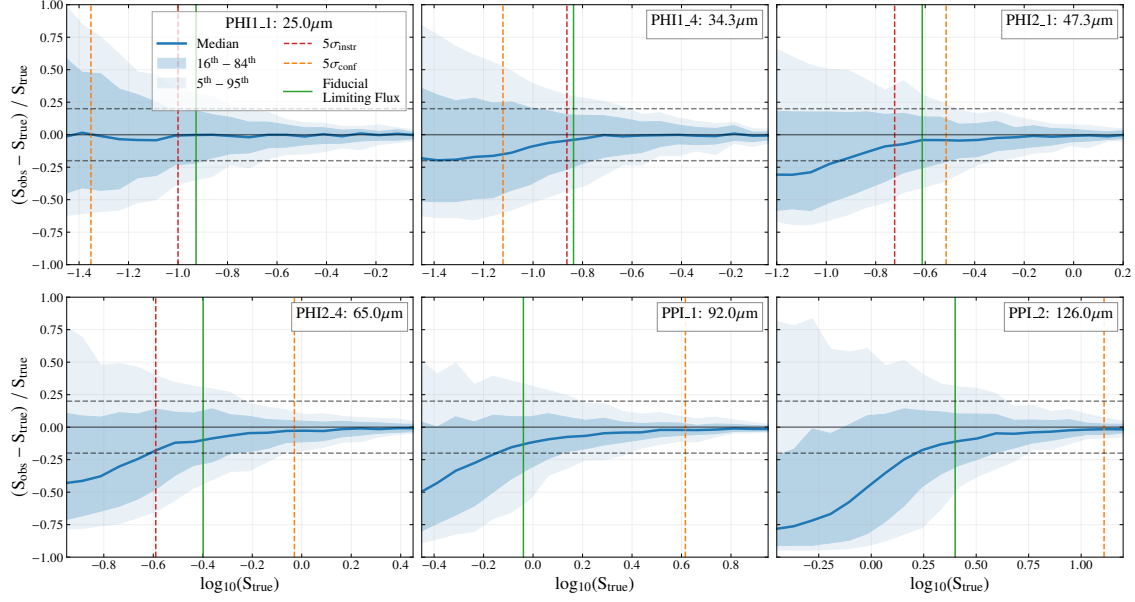


FIG. C1.— Distribution of relative errors between the observed and true fluxes from our fiducial run as a function of the true flux of the sources for a selection of the PRIMAGER bands. These highlight a bias from XID+ to underestimate the flux, which worsens for fainter fluxes and longer wavelength.

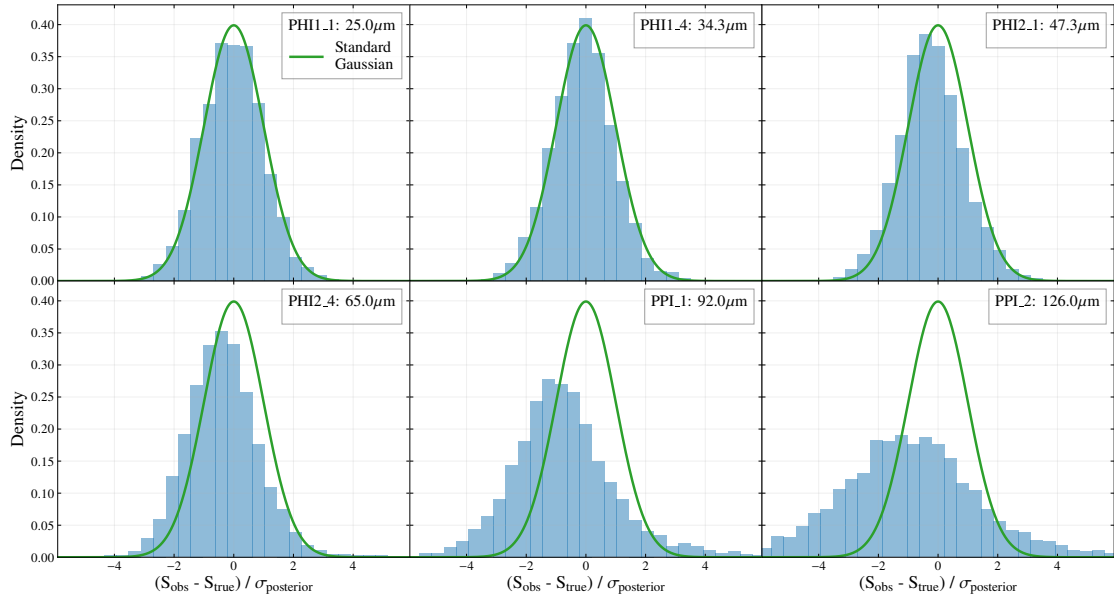


FIG. C2.— Histograms of the differences between the observed and true fluxes from our fiducial run, normalised by the standard deviation of the individual source flux posteriors. The histograms only show sources which have an observed flux above the limiting flux of the fiducial run in the given band. These are compared to a standard normal distribution ($\mu = 0$, $\sigma = 1$). For the longer wavelength channels, the histograms become less Gaussian and show that the spread in the source flux posteriors are underestimated. The bias to underestimate the flux (as shown in Figure C1) is also evident.